

AD-A115 837

PENNSYLVANIA STATE UNIV UNIVERSITY PARK APPLIED RESE--ETC F/G 20/4
BUBBLE DYNAMICS AND RESULTING NOISE FROM TRAVELING BUBBLE CAVIT--ETC(U)
APR 82 R C MARBOE

N00024-79-C-6043

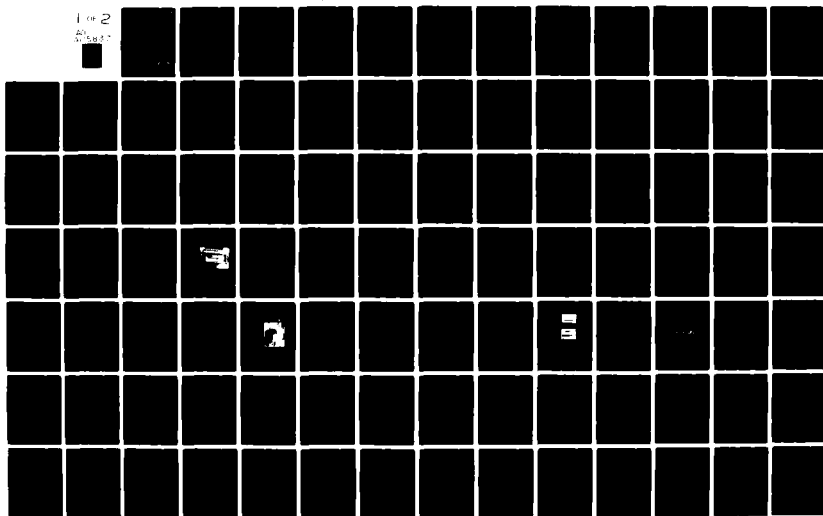
NL

UNCLASSIFIED

ARL/PSU/TM-82-94

1 of 2

AD-A115 837



6

BUBBLE DYNAMICS AND RESULTING NOISE FROM
TRAVELING BUBBLE CAVITATION

R. C. Marboe

Technical Memorandum
File No. TM 82-94
April 13, 1982
Contract No. N00024-79-C-6043

Copy No. 34

The Pennsylvania State University
APPLIED RESEARCH LABORATORY
Post Office Box 30
State College, PA 16801

Approved for Public Release
Distribution Unlimited

NAVY DEPARTMENT
NAVAL SEA SYSTEMS COMMAND

DTIC
S ELECTE
JUN 21 1982
E

AD A115837

DTIC FILE COPY

SECURITY CLASSIFICATION OF THIS PAGE (When Data Entered)

REPORT DOCUMENTATION PAGE		READ INSTRUCTIONS BEFORE COMPLETING FORM
1. REPORT NUMBER TM 82-94	2. GOVT ACCESSION NO. AD-A115837	3. RECIPIENT'S CATALOG NUMBER
4. TITLE (and Subtitle) BUBBLE DYNAMICS AND RESULTING NOISE FROM TRAVELING BUBBLE CAVITATION		5. TYPE OF REPORT & PERIOD COVERED Technical Memorandum
		6. PERFORMING ORG. REPORT NUMBER
7. AUTHOR(s) R. C. Marboe		8. CONTRACT OR GRANT NUMBER(s) N00024-79-C-6043
9. PERFORMING ORGANIZATION NAME AND ADDRESS Applied Research Laboratory Post Office Box 30 State College, PA 16801		10. PROGRAM ELEMENT, PROJECT, TASK AREA & WORK UNIT NUMBERS
11. CONTROLLING OFFICE NAME AND ADDRESS Naval Sea Systems Command Department of the Navy Washington, DC 20362		12. REPORT DATE April 13, 1982
		13. NUMBER OF PAGES 119
14. MONITORING AGENCY NAME & ADDRESS (if different from Controlling Office)		15. SECURITY CLASS. (of this report) UNCLASSIFIED
		15a. DECLASSIFICATION/DOWNGRADING SCHEDULE
16. DISTRIBUTION STATEMENT (of this Report) Approved for public release. Distribution unlimited per NAVSEA - May 12, 1982.		
17. DISTRIBUTION STATEMENT (of the abstract entered in Block 20, if different from Report)		
18. SUPPLEMENTARY NOTES		
19. KEY WORDS (Continue on reverse side if necessary and identify by block number) travelling, bubble, cavitation, noise, thesis		
20. ABSTRACT (Continue on reverse side if necessary and identify by block number) The acoustic noise spectrum associated with traveling bubble cavitation on a Schiebe headform in a variable pressure water tunnel was measured over the 2.5 to 80 kHz frequency range. Bubble dynamics were observed through video taping and the nuclei distribution was obtained holographically.		

20. Observed noise spectra showed that low frequency noise can be modeled by incompressible theory. High frequency noise, apparently resulting from a shock wave, can be modeled by compressible theory. The spectrum was seen to shift toward lower frequencies than predicted possibly due to axisymmetric bubble collapse.

The spectral energy per bubble was experimentally derived and was found to be a reasonable approximation to that predicted by incompressible theory over the cavitation number range tested.

The collapse peak pressure amplitude distribution, the maximum bubble radius distribution and the nuclei distribution were all found to be lognormal.

LB

ABSTRACT

The acoustic noise spectrum associated with traveling bubble cavitation on a Schiebe headform in a variable pressure water tunnel was measured over the 2.5 to 80 kHz frequency range. Bubble dynamics were observed through video taping and the nuclei distribution was obtained holographically.

Observed noise spectra showed that low frequency noise can be modeled by incompressible theory. High frequency noise, apparently resulting from a shock wave, can be modeled by compressible theory. The spectrum was seen to shift toward lower frequencies than predicted possibly due to asymmetric bubble collapse.

The spectral energy per bubble was experimentally derived and was found to be a reasonable approximation to that predicted by incompressible theory over the cavitation number range tested.

The collapse peak pressure amplitude distribution, the maximum bubble radius distribution and the nuclei distribution were all found to be lognormal.



Accession For	
NTIS GRA&I	<input checked="" type="checkbox"/>
DTIC TAB	<input type="checkbox"/>
Unannounced	<input type="checkbox"/>
Justification	
By	
Distribution/	
Availability Codes	
Dist	Avail and/or Special
A	

TABLE OF CONTENTS

ABSTRACT	Page 2
LIST OF FIGURES	5
LIST OF TABLES	8
LIST OF SYMBOLS	9
ACKNOWLEDGMENTS	12
Chapter	
1. INTRODUCTION	13
1.1 Historical Background	13
1.2 Objectives of Study	16
2. THEORY	19
2.1 Single Bubble Analysis	19
2.1.1 Incompressible Theory	20
2.1.2 Compressible Theory	28
2.1.3 Asymmetric Bubble Collapse	31
2.2 Scaling Factors	34
3. PROCEDURE	38
3.1 The 12 Inch Diameter Water Tunnel	38
3.2 Model	40
3.3 Air Content	45
3.4 Measurement of Pressure and Velocity	45
3.5 Measurement of Cavitation Inception and Desinence	46
3.6 Noise Measurement	48
3.7 Recording Bubble Dynamics	52
3.8 Measurement of Gas Nuclei in Water	52

TABLE OF CONTENTS (continued)

	Page
4. RESULTS	58
4.1 Cavitation Characteristics	58
4.2 Single Bubble Cavitation Noise	61
4.3 Low Frequency Characteristics	77
4.4 Analysis of Bubble Dynamics	82
4.5 Correlation of Bubble Dynamics with Noise Spectra Levels	87
4.6 Correlation of Bubble Dynamics with Nuclei	91
5. SUMMARY	95
5.1 Discussion	95
5.2 Conclusions	100
REFERENCES	103
APPENDIX A. FRAUNHOFER HOLOGRAPHY	108
APPENDIX B. DATA ACQUISITION SYSTEM SENSITIVITY APPLICATION TO ACOUSTIC SPECTRA	113

LIST OF FIGURES

Figure	Page
1. Schematic of 12 Inch Diameter Water Tunnel	39
2. Schiebe Body Mounted in Test Section	42
3. Interpolated Values of Coefficient of Pressure versus Surface Position on Schiebe Body	43
4. Configuration of Hydrophone in Water Tank Used to Measure Cavitation Noise	49
5. Schematic Diagram of Instrumentation for Cavitation Noise Spectra	51
6. Schematic Diagram of Instrumentation for Cavitation Bubble Count and Noise Data	53
7. Schematic Drawing of Video Taping Apparatus	54
8. Enclosure for Holography	57
9. Cavitation Numbers for Inception and Desinence of Traveling Bubble Cavitation and Inception of an Attached Cavity as a Function of U_{∞}	60
10. Hydrophone Response to a.) 1 Cycle of a 25 kHz Sinusoid and b.) 16 Cycles of a 25 kHz Sinusoid Source Input on Model Surface at Approximate Location of Bubble Collapse.	62
11. Example of Cavitation Noise Signal for $U_{\infty} = 37.5$ fps and $\sigma = .74$	64
12. Noise Burst Interval Distribution	65
13. Nondimensional Number of Bubble Collapses per Second versus Cavitation Number for Velocities $U_{\infty} = 30.0$ fps and $U_{\infty} = 37.5$ fps	67
14. Nondimensional Sound Pressure Level versus Cavitation Number for Velocities $U_{\infty} = 30.0$ fps and $U_{\infty} = 37.5$ fps	68

LIST OF FIGURES (continued)

Figure	Page
15. Cavitation Noise Level per Bubble versus Cavitation Number for Velocities $U_{\infty} = 30.0$ fps and $U_{\infty} = 37.5$ fps.	69
16. Spectrum Averaging Process	73
17. Averaged Traveling Bubble Cavitation 80 kHz Noise Spectra for $U_{\infty} = 30.0$ fps	74
18. Averaged Traveling Bubble Cavitation 80 kHz Noise Spectra for $U_{\infty} = 37.5$ fps	75
19. Averaged Traveling Bubble Cavitation 16 kHz Noise Spectra for $U_{\infty} = 30.0$ fps	78
20. Averaged Traveling Bubble Cavitation 16 kHz Noise Spectra for $U_{\infty} = 37.5$ fps	79
21. Averaged Traveling Bubble Cavitation 8 kHz Noise Spectra for $U_{\infty} = 30.0$ fps	80
22. Averaged Traveling Bubble Cavitation 8 kHz Noise Spectra for $U_{\infty} = 37.5$ fps	81
23. Maximum Cavitation Bubble Radius Distribution for $U_{\infty} = 30.0$ fps and $\sigma = .80$	84
24. Maximum Cavitation Bubble Radius Distribution for $U_{\infty} = 30.0$ fps and $\sigma = .68$	85
25. Cavitation Bubble Collapses per Second versus Peak Pressure Amplitude for $U_{\infty} = 30.0$ fps and $\sigma = .80$	88
26. Cavitation Bubble Collapses per Second versus Peak Pressure Amplitude for $U_{\infty} = 30.0$ fps and $\sigma = .68$	89
27. Peak Pressure Amplitude versus Maximum Bubble Radius for $U_{\infty} = 30.0$ fps and $\sigma = .68$	90
28. Nuclei Distribution for $U_{\infty} = 30.0$, $\sigma = .80$ and Total Air Content of 8.5 ppm	92

LIST OF FIGURES (continued)

Figure	Page
29. Nuclei Distribution for $U = 30.0$ fps, $\sigma = .68$ and Total Air Content of 8.5 ppm	93
30. Comparison of Experimental Results of Hamilton (24) and Present Study to Incompressible Theory for Traveling Bubble Cavitation Noise.	98
A1. Schematic Drawing of Holocamera	109
A2. Schematic Drawing of Reconstruction and Viewing System	112
B1. LC-10 Free Field Transmitting Response	116
B2. Hydrophone Receiving Response Spectrum	117
B3. Sensitivity Spectrum	118
B4. Typical Cavitation Noise Spectrum	119

LIST OF TABLES

Table	Page
1. Equations Defining the Coefficient of Pressure on the Surface of the Schiebe Body	44
2. Functional Relationships for the Dependence of N , L , L_B on σ	70
3. Bin Sizes for Holographic Nuclei Distributions. . .	94

LIST OF SYMBOLS

a	radius of Schiebe body
c	speed of sound
C_p	pressure coefficient
$C_{p_{min}}$	minimum pressure coefficient
d	distance travelled by bubble with $P < P_v$
f	frequency
k	exponent
H	specific enthalpy
\dot{H}	first time derivative of H
H_M	enthalpy at maximum bubble radius
L	noise level
L_B	noise level per bubble
M	acoustic Mach number
N	number of noise bursts per second
p	acoustic pressure
P	pressure
P_G	noncondensable gas pressure
P_L	liquid pressure at bubble interface
P_m	pressure at minimum radius
P_o	stagnation pressure
P_s	peak shock wave pressure
P_v	vapor pressure
P_∞	free stream static pressure

Q	partial gas pressure
r	radial coordinate
R	bubble radius
\dot{R}, \ddot{R}	first and second time derivatives of R
R_m	minimum bubble radius
R_n	bubble radius at collapse initiation
R_M	maximum bubble radius
R_0	initial bubble radius
s	arc length
S	spectral energy density
t	time
T	time period
u	radial velocity
U_∞	free stream velocity
V	bubble volume
\ddot{V}	second time derivative of V
x	axis of rotation coordinate
θ	time constant
γ	specific heat ratio
λ	statistical parameter
ξ	retarded time $(t-r/c)$
ν	kinematic viscosity
ρ	mass density
σ	cavitation number
σ_d	desinent cavitation number

σ_i	incipient cavitation number
σ_{st}	surface tension
τ	bubble lifetime
τ_c	duration of bubble collapse
τ_g	duration of bubble growth

ACKNOWLEDGMENTS

The entire staff of the Garfield Thomas Water Tunnel is acknowledged for their invaluable assistance throughout this project. The author is especially grateful to the members of the Computer Group for their support. This thesis would not have been possible without the insight and guidance of Dr. Patrick Leehey of the Massachusetts Institute of Technology and the advice and encouragement of Drs. Donald E. Thompson and Michael L. Billet.

This research was supported by the Applied Research Laboratory of the Pennsylvania State University under contract with the United States Naval Sea Systems Command.

Chapter 1

INTRODUCTION

1.1 Historical Background

Cavitation is the rupture of a liquid or a liquid-solid interface caused by reduction of local static pressure below the vapor pressure of the fluid medium. This rupture manifests itself as a macroscopic bubble. Microscopic voids present in liquids act as seeds or nuclei for cavitation bubbles (1).

Cavitation is a prominent source of noise in underwater acoustics. It is basically a monopole source due to volume changes but some dipole and quadrupole components are present from asymmetries in the bubble shape.

When bubbles created by hydrodynamic cavitation are moved by the flow out of the region where the static pressure is less than vapor pressure, the vapor condenses quickly as the pressure rises resulting in the collapse of the bubble. The violence of this collapse produces a high amplitude pressure wave which propagates into the medium as sound. The collective intensity of thousands of bubble collapses per second for well developed traveling bubble cavitation is such that a major noise source is produced.

The study of the mechanism of noise production by a

collapsing bubble has resulted in several theories and models based upon numerous assumptions since Besant (2) first discussed the calculation of the pressure field caused by the collapse of a spherical cavity in an incompressible fluid in 1859.

The first significant breakthrough came in 1917 when Lord Rayleigh (3) calculated the pressure field around a vacuum cavity and predicted the collapse time. But, because the cavity was assumed to be a void, an infinite wall collapse velocity was predicted as the cavity radius approached zero.

The next logical step was to introduce the effect of vapor inside the cavity recognizing it as a source of limitation to the wall acceleration. As the wall velocity does approach the speed of sound however, the effect of liquid compressibility has to be accounted for. In 1952, Gilmore (4) used the Kirkwood-Bethe approximation to model the final collapse period where liquid compressibility is a factor. Mellen (5) substituted the use of Gilmore's theory for final collapse and calculated the resultant shock wave pressure as a time function. The development of a shock wave theory was furthered by Willard (7). He also observed that a produced shock wave would influence the growth of nearby nuclei.

The effect of surface tension on the collapse was shown by Bahl and Ray (6) to be significant only when the maximum

bubble radius was of very small magnitude. They found that this effect was not significant in water.

As theories developed for predicting bubble collapse times and velocities, the next major area of investigation was the sound power spectrum produced. Mellen (8) experimentally derived a spectrum and in 1956 Fitzpatrick and Strasberg (9) predicted a peak in the noise spectrum at the frequency determined by the reciprocal of the Rayleigh collapse time. Also, they used the Rayleigh analysis to derive the far field acoustic pressure as a function of the second time derivative of the bubble volume. Blake, et. al. (10) used these single bubble analyses to scale experimentally derived spectra.

More recent investigations have focused on the role of the nuclei in cavitation inception and scaling. Van der Walle (11), Apfel (12), and Lauterborn (13) have all tried to explain cavitation inception scaling in terms of nuclei composition and dynamics. Keller (14) and later Gates, et. al. (15) used light scattering and holographic methods to study the relationship of nuclei distribution to cavitation inception. Oldenziel (16) did a study of what he called cavitation susceptibility and of cavitation bubble size.

Models grew more complex as idealizations were replaced by natural parameters. Numerical solutions became possible as computers were made more powerful and affordable. Hickling and Plesset (17) did a numerical analysis of the

collapse of a gas filled bubble in a compressible fluid in 1964. Morozov (18) used a statistical analysis to determine the conditions under which single bubble theory could be used.

The most recent adaptation of single bubble analysis is the investigation of the effect of the collapse of asymmetric bubbles. Since cavitation often occurs near a solid boundary, this is of significance. Rayleigh assumed a spherical cavity and axisymmetric collapses. But bubbles collapse in a toroidal shape forming water jets when in the proximity of a solid surface. This phenomenon has been investigated by Plesset and Chapman (19), Hsieh (20), Kozyrev (21), and Mitchell and Hammitt (22). The use of high speed computers has resulted in models which agree well with bubble dynamics recorded by high speed film. Chahine, et. al. (23) incorporated asymmetric bubble collapse into a correlation of noise and cavitation bubble dynamics in 1979.

An investigation of bubble dynamics and the use of single bubble theory to experimentally determine the noise per bubble collapse was conducted by Hamilton (24). He found experimental data which indicated that a combination of theories was necessary to describe the bubble dynamics and sound power spectrum.

1.2 Objectives of Study

Most previous cavitation studies have focused on either

single bubbles generated by sparks or developed body cavitation types such as vortex and sheet. This study is a blend of these approaches. Traveling bubble cavitation lends itself to modeling by single bubble theory yet also is subjected to near-solid collapse effects which are prominent in many natural applications.

The noise for traveling bubble cavitation has been found to be more intensive than that from frothy cavitation. The intensity of the noise from traveling bubble cavitation is determined by the collective intensity of many unique bubble collapses. Because of this, single bubble analysis is justified. However, several theoretical models exist for predicting the noise produced by the collapse of a single bubble. This study will investigate the applicability of each model over the frequency spectrum of the noise. The role of asymmetric collapse of the bubble due to proximity to a solid boundary will also be discussed.

This study comprises five areas of investigation.

The dependence of the noise upon flow variables such as free-stream pressure and velocity is examined. The shape of the sound power spectra is examined to determine the frequency ranges of noise production. A third area of investigation is a determination of the noise contribution of each bubble by measuring the total noise level and the number of bubbles involved. Previous investigations

(3,32,35) have concluded that the maximum radius of the vaporous cavitation bubble is a key parameter in the determination of the spectral density of the emitted noise. Therefore, the relationship of the peak pressure level produced by a collapsing bubble and its maximum radius is investigated. Also, several recent studies have shown an important relationship between the nuclei size and cavitation (11,12,14,15). Hence, it is important that the fifth area of study be the examination of the relationship between the experimentally determined maximum bubble radius distribution for a given flow condition and the nuclei distribution.

The overall objective of this study is to apply the idealized theories developed from studies of the collapse and emission of sound by spherical bubbles created artificially by spark gaps and lasers to the asymmetric bubbles of body cavitation encountered in practice.

Chapter 2

THEORY

2.1 Single Bubble Analysis

The analytical techniques used to date to study traveling bubble cavitation are predicated upon the veracity of scaling single bubble dynamics for high collapse rates. In order to justify the use of single bubble analysis, the condition of independence of collapse rates must be satisfied. Therefore, bubbles should not exist in such a proximity that they have an effect upon each other.

The statistical treatment of cavitation noise has been particularly popular in the Soviet Union. Levkovskii (25) found that the distribution of time intervals between successive collapses was exponential. Given an exponential distribution for time intervals with a parameter of λ for example, the distribution of event occurrences will be a Poisson distribution with mean rate λ (26). Akulichev and Ol'shevskii (27) studied the statistical characteristics of cavitation noise using the theory of Poisson processes to theoretically develop a continuous energy spectra. Also, based upon a Poisson distribution of random collapses, Morozov (18) modeled cavitation noise as an aperiodic train of pulses of varying amplitude and occurrence rate.

Therefore, the spectrum of a single bubble collapse would be similar to the spectrum resulting from a collection of random collapses.

Supported by experimental data, these theories are employed to justify the investigation of single bubble dynamics and noise production which is the basis of this study.

The energy density spectrum of a single bubble collapse can be derived from the power spectrum of the cavitation noise. Rice (28) showed that the energy density spectrum is proportional to the power spectrum for shot effect noise such as traveling bubble cavitation. He demonstrated that the total noise power is equal to the number of bubble collapses per second times the energy per bubble.

2.1.1 Incompressible Theory

The first solution to the problem of determining the fluid response to the annihilation of a spherical void in a compressible fluid was done by Lord Rayleigh (3). His solution was based upon several assumptions including:

- an incompressible fluid,
- uniform pressure and temperature in the cavity,
- the cavity and surrounding flow field are spherically symmetrical,
- heat conduction, surface tension, and viscosity factors are negligible,

- body forces are zero.

Let us first trace the growth of such a cavity. The velocity potential for a spherically expanding surface is given by

$$\phi = \frac{R^2 \dot{R}}{r} \quad (1)$$

where R is the bubble radius at a given time and $\dot{R} = dR/dt$ is the wall velocity. For an irrotational motion of an incompressible fluid, the equation of motion is generally given by

$$\text{grad} \left[\frac{P}{\rho} + \frac{1}{2} (\nabla \phi)^2 - \frac{\partial \phi}{\partial t} \right] = 0 \quad (2)$$

where $P(r,t)$ is the instantaneous pressure and ρ is the mass density of the fluid. In the fluid, the following applies for an expanding sphere:

$$\frac{P(r)}{\rho} + \frac{1}{2} \left(\frac{R^2 \dot{R}}{r^2} \right)^2 - \left(\frac{2R\dot{R}^2 + R^2 \ddot{R}}{r} \right) = \frac{P_\infty}{\rho} \quad (3)$$

The effects of surface tension and viscosity are negligible compared to the terms in Equation (3). The pressure drop due to surface tension is given by

$$\Delta P = \frac{2\sigma_{st}}{R} \quad (4)$$

where σ_{st} is the surface tension. The viscous term is

$$\frac{4\nu}{R} \dot{R} \quad (5)$$

where ν is the kinematic viscosity.

At the interface of the cavity, $r=R$, Equation (3) becomes

$$\ddot{R}R + \frac{3}{2} \dot{R}^2 = \frac{1}{2R^2} \frac{d}{dt} (R^3 \dot{R}^2) = \frac{P(R) - P_\infty}{\rho} = \frac{P}{\rho} \quad (6)$$

where P_∞ is the fluid equilibrium pressure far from the cavity. Integrating this equation and assuming the pressure at the interface to be constant during growth gives

$$R^3 \dot{R}^2 = \frac{2}{3} \frac{P}{\rho} (R^3 - R_0^3) \quad (7)$$

where R_0 is the initial cavity radius. The wall velocity and acceleration were found from Equation (7) to be

$$\dot{R} = \left[\frac{2}{3} \frac{P}{\rho} \left| 1 - \frac{R_0^3}{R^3} \right| \right]^{1/2} \quad (8)$$

and

$$\ddot{R} = \frac{PR_0^3}{R^4 \rho} \quad (9)$$

Equation (6) is known as the Rayleigh-Plesset equation. It can be put in terms of volume dynamics instead of radius dynamics as follows

$$P(r,t) = \frac{\rho}{r} (R^2 \ddot{R} + R \dot{R}^2) \quad (10)$$

$$= \frac{\rho}{3r} \frac{d^2}{dt^2} (R^3) \quad (11)$$

$$= \frac{\rho}{4\pi r} \ddot{V}(\xi) \quad (12)$$

where $\xi = t - r/c$ is a retarded time dependent upon the speed of sound in the fluid. An inner incompressible flow generates an outer acoustic field. The latter does not react back on the former to affect the first order volume velocity, \dot{V} . This is plausible because the Schiebe body source is considered to be compact. That is, the equivalent radius of the volume source is small compared to the

acoustic wavelength. The inner and outer flows can be described by matched asymptotic expansions for the boundary-value problem. As described by Pierce (29), both expansions represent solutions of the Helmholtz equation. The outer expansion terms must also satisfy the Sommerfield radiation condition. The inner expansion for a compact source is given by

$$\frac{S}{r} - D \cdot \nabla \frac{1}{r} + \sum_{j,k}^3 Q_{jk} \frac{\partial^2}{\partial x_j \partial x_k} \frac{1}{r} - \dots \quad (13)$$

where the three terms are the monopole, dipole, and quadrupole contributions respectively. The outer expansion is expressed as

$$\frac{S(t-r/c)}{r} - \nabla \cdot \frac{D(t-r/c)}{r} + \sum_{j,k}^3 \frac{\partial^2}{\partial x_j \partial x_k} \frac{Q_{jk}(t-r/c)}{r} \quad (14)$$

It is the acoustic field which is described by the compressible theory expression of Equation (12).

It has been found useful to express the pressure in terms of two non-dimensional numbers. The coefficient of pressure is used in hydrodynamics to normalize the pressure near a body. It is given by

$$C_p = \frac{P - P_\infty}{\frac{1}{2} \rho U_\infty^2} \quad (15)$$

where P is the local pressure at the point of interest and P_∞ and U_∞ are the free-stream pressure and velocity respectively. The cavitation number is defined as

$$\sigma = \frac{P_\infty - P_v}{\frac{1}{2} \rho U_\infty^2} \quad (16)$$

where P_v is the vapor pressure of the fluid.

After a period of rapid initial growth, the bubble grows at a fairly constant rate as indicated by Equation (8). Thus, Equation (8) reduces to

$$\dot{R} = \left[\frac{2}{3\rho} (P_v - P) \right]^{1/2} \quad (17)$$

when P_∞ is replaced by the local pressure P that would exist if the bubble was not present and $P(R)$ is replaced by its dominant component, P_v . Substitution of non-dimensional terms in Equation (17) gives

$$\dot{R} = U_\infty \left[-\frac{1}{3} (\overline{C_p} + \sigma) \right]^{1/2} \quad (18)$$

Assuming relatively constant growth, a maximum radius, R_M , can be determined from the product of growth rate and the time of growth defined as the period in which the bubble is in the region $P < P_v$. This time is defined as

$$\tau_g = \frac{d}{U_\infty (1 - \overline{C_p})^{1/2}} \quad (19)$$

where d is the linear path of the bubble through the $P < P_v$ region and $\overline{C_p}$ is the average coefficient of pressure in that region. The product of Equations (18) and (19) is

$$R_M = d \left[\frac{1}{3} \frac{(\overline{C_p} + \sigma)}{(\overline{C_p} - 1)} \right]^{1/2} \quad (20)$$

Baiter (30) modified Equation (20) to account for inertial effects after the bubble leaves the low pressure region. This gives

$$R_M = d \left[\frac{1}{3} \frac{(\overline{C_p} + \sigma)}{(\overline{C_p} - 1)} \right]^{1/2} \left[\frac{\overline{C_{p1}} - \overline{C_p}}{\overline{C_p} + \sigma} \right]^{1/3} \quad (21)$$

where $\overline{C_{p1}}$ is the average pressure encountered by the bubble

as it enters the high pressure region that will initiate collapse.

Rayleigh derived the wall velocity during collapse from equating the sum of the potential and kinetic energies during collapse to the potential energy of the bubble at maximum volume. This yielded

$$\frac{4}{3} \pi R^3 P + 2\pi \rho R^2 \dot{R}^2 = \frac{4}{3} \pi R_M^3 P \quad (22)$$

This gives a wall velocity of

$$\dot{R} = \left[\frac{2}{3} \frac{P}{\rho} \left(\frac{R_M^3}{R^3} - 1 \right) \right]^{1/2} \quad (23)$$

For other than the initial and final stages of collapse, Equation (23) simplifies to

$$\dot{R} = \left[\frac{2}{3} \frac{P}{\rho} \left(\frac{R_M}{R} \right)^3 \right]^{1/2} = U_\infty \left[\frac{1}{3} (C_p + \sigma) \right]^{1/2} \left[\frac{R_M}{R} \right]^{3/2} \quad (24)$$

Rayleigh found the time of collapse to be

$$\tau_c = 0.915 R_M \sqrt{\frac{\rho}{P}} = 0.915 \frac{R_M}{U_\infty} \sqrt{\frac{2}{\sigma}} = 1.3 \frac{R_M}{U_\infty (C_p + \sigma)^{1/2}} \quad (25)$$

The limit of Equation (24) as the bubble collapses towards a zero radius is seen to be infinite velocity. Physical reality dictates otherwise. The presence of a permanent gas in the bubble results in use of the wall kinetic energy to compress the gas resulting in a termination of collapse before $R = 0$.

Assuming adiabatic compression of the gas, Noltingk and Neppiras (31) derived an equation for the wall velocity of a partially gas filled bubble in an ideal, incompressible,

inviscid fluid. That equation of motion is

$$\ddot{R}R + \frac{3}{2} \dot{R}^2 = \frac{P}{\rho} \left[1 + \frac{Q}{P} \left(\frac{R_M}{R} \right)^{3\gamma} \right] \quad (26)$$

where γ is the adiabatic exponent and Q is the partial gas pressure. From this, the wall velocity was found to be

$$\dot{R} = \frac{2}{3} \frac{P}{\rho} \left(\frac{R_M}{R} \right)^3 \left[1 - \left(\frac{R}{R_M} \right)^3 + \frac{Q}{P(\gamma-1)} \left(1 - \frac{1}{\gamma-1} \left(\frac{R_M}{R} \right)^{3(\gamma-1)} \right) \right] \quad (27)$$

By setting $R = 0$, a minimum radius is found from

$$R_m = R_M \left[\frac{Q}{P(\gamma-1)} \right]^{\frac{1}{3(\gamma-1)}} \left[1 + \frac{Q}{P(\gamma-1)} \right]^{-\frac{1}{3(\gamma-1)}} \quad (28)$$

For an average value of $\gamma = 4/3$, Equations (27) and (28) reduce to

$$\dot{R} = \frac{2P}{3\rho} \left(\frac{R_M}{R} \right)^3 \left[1 - \left(\frac{R}{R_M} \right)^3 + \frac{3Q}{P} \left(1 - \frac{3R_M}{R} \right) \right] \quad (29)$$

and

$$R_m = R_M \left(\frac{3Q}{P} \right) \left(1 + \frac{3Q}{P} \right)^{-1} \quad (30)$$

A maximum Mach number in liquid was also derived for the Noltingk-Neppiras incompressible equation as

$$M_{\max} = \left[\frac{2P}{3\rho c^2} \left(\frac{\gamma-1}{\gamma} \right) \right]^{1/2} \left[\frac{P(\gamma-1)}{Q\gamma} \right]^{\frac{1}{2(\gamma-1)}} \left[1 + \frac{Q\gamma}{P(\gamma-1)} \right]^{\frac{\gamma}{2(\gamma-1)}} \quad (31)$$

This is an overestimation for Mach numbers greater than 0.3.

A reasonable approximation for the maximum Mach number is given by

$$M_{\max} = \left(0.015 \frac{R_M}{R_m} \right)^{3/2} P_{\infty}^{1/2} \quad (32)$$

where P_{∞} is measured in atmospheres for $R_m/R_M < 0.25$.

To find the produced pressure predicted by Equation (12), Rayleigh's theory and the Noltingk-Neppiras result for

the minimum radius were used to derive the volume acceleration during the bubble collapse phase. That yielded

$$\ddot{V} = - 2\pi \sqrt{\frac{2P}{3\rho}} \left(\frac{R_M}{R}\right)^{3/2} \frac{\left(1 - 4\left(\frac{R}{R_M}\right)^3\right)}{\left(1 - \left(\frac{R}{R_M}\right)^3\right)^{1/2}} R \dot{R} \quad (33)$$

Substitution of Equation (33) into Equation (12) gives the instantaneous acoustic pressure as

$$P(t) = \frac{PR_M^3}{3rR^2} \left(1 - 4\left(\frac{R_m}{R_M}\right)^3\right) \quad (34)$$

The peak positive acoustic pressure is

$$P_{\max} = \frac{P}{3} \frac{R_M^3}{rR_m^2} \left(1 - 4\left(\frac{R_m}{R_M}\right)^3\right) \quad (35)$$

Less than 1% of the radiated energy is due to the bubble growth phase (1); hence, Equation (34) is considered to be a reasonable approximation of acoustic pressure produced by spherical cavitation bubble collapse in an incompressible fluid.

The acoustic spectral energy density is found by first substituting Equation (24) into Equation (11) to give

$$P(r,t) = \left(\frac{\rho}{r}\right) U_\infty^{1.2} R_M^{1.8} (C_p + \sigma)^{0.6} t^{-0.8} \quad (36)$$

followed by taking the Fourier transform and squaring its absolute value to finally yield

$$S(f) \sim \left(\frac{\rho}{r}\right)^2 U_\infty^{2.4} R_M^{3.6} (C_p + \sigma)^{1.2} f^{-0.4} \quad (37)$$

2.1.2 Compressible Theory

Incompressible theory has been demonstrated to be adequate for most of the bubble growth and collapse time period. But, in the final collapse stage, the wall velocity exceeds the speed of sound so the liquid can't be considered incompressible any longer. Also the presence of gas filled nuclei increases the effective fluid compressibility. The effect of compressibility is to limit the wall motion thus reducing the wall velocity. Compressibility limits the fluid inertia associated with the collapse.

Because an exact analytic solution cannot be found, numerical solutions have been done. Flynn (32) outlined several approximations which modify the Rayleigh-Plesset equation for the effects of compressibility. The one which applies to the final stage of collapse is the Kirkwood-Bethe approximation. Using this approximation, Gilmore (4) derived a modified Rayleigh-Plesset equation as follows

$$\left(1 - \frac{\dot{R}}{C}\right)\ddot{R} + \frac{3}{2} \left(1 - \frac{\dot{R}}{3C}\right) \frac{\dot{R}^2}{R} = \left(1 - \frac{\dot{R}}{C}\right) \frac{H}{R} + \left(1 - \frac{\dot{R}}{C}\right) \frac{\dot{H}}{C} \quad (38)$$

where H is the specific enthalpy and C is the speed of sound in the liquid at the bubble interface. Flynn (33) reviewed the numerical solutions done by Hickling and Plesset (17) and Ivany and Hammitt and found that the Gilmore equation was a good approximation to experimental observations. The Hickling and Plesset analysis took the solution beyond the final collapse into the region where the bubble rebounds and

generates a shock wave.

The wall velocity is given by

$$R = \left\{ \frac{2}{3} |H_M| \left[\frac{R_n^3}{R} \left(1 - \frac{\dot{R}}{3C} \right) - 1 \right] \right\}^{1/2} \quad (39)$$

where H_M is the specific enthalpy at the maximum bubble radius and R_n is the bubble radius when the collapse initiates. Equations for the specific enthalpy for water and the speed of sound at the bubble wall are given by Cramer (34) as

$$H = \int_{P_\infty}^{P(R)} \frac{dP}{\rho} = \frac{7}{6} \frac{(3001 \text{ atm})^{1/7}}{\rho} \{ (P(R) + 3000 \text{ atm})^{6/7} - (P_\infty + 3000 \text{ atm})^{6/7} \} \quad (40)$$

and

$$C = (C_0^2 + 6H)^{1/2} \quad (41)$$

where C_0 is given for water as 1482 m/s.

Esipov and Nauqol'nykh (35) estimated the maximum wall velocity as

$$\dot{R}_{\max} = -0.6 C \left(\frac{P_m}{\rho C^2} \right)^{5/7} \quad (42)$$

where P_m is the pressure at the interface at the minimum bubble radius.

Gilmore derived the pressure field as

$$P(r,t) = \frac{R}{r} (P_2 + P_\infty) + \frac{R}{r} \left(1 - \frac{R^3}{r^3} \right) \left(\frac{1}{2} \rho \dot{R}^2 \right) + \frac{r \dot{R}}{C} \left(1 - \frac{R}{r} \right) \left[\rho \dot{R}^2 - 2(P_2 - P_\infty) - R \frac{dP_2}{dR} \right] \quad (43)$$

identifying the first two terms as the nonradiated induced pressure and the last term as the radiated acoustic

pressure.

When the bubble collapses, inertial forces in the surrounding fluid develop rapidly increasing kinetic energy that is either stored in the compressible fluid or converted into internal energy of the bubble gas. The inward wall motion is arrested by the bubble internal pressure and part of the stored energy is radiated as a shock wave from the rebounding bubble (36).

Benjamin (37) predicted a maximum shock wave pressure of

$$P_s > 13.6 \left[\log \left(\frac{r}{R_m} \right) \right]^{-2/3} \quad (44)$$

where P_s is in kilobars (10^5 kPa).

Esipov and Naugol'nykh (34) developed an equation describing the shock wave emitted considering compressibility and the presence of a noncondensable gas in the bubble. The shock wave is assumed to be of the exponential form $P_s(r,t) = P_s e^{-t/\theta}$. Assuming $\gamma = 4/3$ for water this approximation is given by

$$P_s(r,t) = P_m R_m \left[r M^{3/2} \left(2 \ln \frac{r}{R_m} \right)^{1/2} \right]^{-1} e^{-t/\theta} \quad (45)$$

$$= \frac{1}{\sqrt{2}} \rho c^2 \frac{R_m}{r} \left[\frac{P_G}{\rho c^2} \right]^{1/4} \left[\ln \frac{c}{R_m} \right]^{-1/2} e^{-t/\theta} \quad (46)$$

where θ is given by

$$\theta = \frac{R_m}{c} \left[\frac{P_G}{\rho c^2} \right]^{1/4} M^{-3/2} \left[1 + 2\sqrt{2} M^{3/2} \left(\ln \frac{r}{R_m} \right)^{1/2} \right]. \quad (47)$$

The minimum radius is related to the maximum radius by

$$R_m = R_M M^{-1/2} \left[\frac{P_G}{\rho c^2} \right]^{1/4} \quad (48)$$

and the acoustic Mach number is given by

$$M = \left[\frac{1}{2} + \frac{3P_G^{3/4} (\rho c^2)^{1/4}}{P} \right]^{-1} \quad (49)$$

These equations are valid in water for $P_s \gg p c^2 / 7$ and $r \gg R_m \exp (M^{3/4})$.

The generation of the shock wave is modeled as a pressure impulse. The pressure given by Equation (45) when squared and the Fourier transform taken yields an energy density spectrum of

$$S(f) = \frac{(P_s \theta)^2}{1 + (2\pi \theta f)^2} \quad (50)$$

This spectrum is approximately flat to $1/2\pi\theta$ then rolls off at a rate of f^{-2} .

2.1.3 Asymmetric bubble collapse

So far, all of the described theories have assumed a spherical shape for the collapsing bubble. In practice, interest is often focused on cavitation near a solid surface. In this case, the effect of proximity to a solid is enough to cause asymmetric collapse of the cavity. Many investigations have been concerned with the water jet formed in such an asymmetric collapse (21,38,39). It is believed that this is a primary mechanism of cavitation damage. Very

little has been done to study the effect of the asymmetric bubble dynamics upon the production of cavitation noise. The neglect of the study of nonspherical bubbles is not due to lack of recognition of the problem; rather, the difficulty in modeling a nonspherical motion has prevented the derivation of an exact solution. Therefore most of the work done in the area of nonspherical bubble dynamics has been numerical analysis.

Plesset (40) has found that theory exaggerates the importance of the liquid inertia term ($3/2 \dot{R}^2$ term in Equation 6) for the final stage of the collapse of a bubble near a solid surface.

The modeling of the nonspherical collapse dynamics began with assuming slight deviation from sphericity. The results could be linearized by assuming the amplitudes of the spherical harmonics were small. The next step was to introduce nonlinearities from large deviations.

Blake and Gibson (41) modeled the early stages of collapse by adapting a distribution of sources and derivatives (e.g. doublets) along the axis of symmetry inside the bubble. This technique failed to adequately describe the final stages of collapse because of a restriction in the resolution of the surface shape due to a decrease in the center line length.

Mitchell and Hammitt (22) and Plesset and Chapman (38) used the Marker and Cell finite difference approach to model

this final collapse stage. Lauterborn and Bolle (42) found good experimental agreement with the results of Plesset and Chapman in addition to the formation of a strong shock wave on the collapse of a bubble in proximity to a solid boundary.

Extremely complex theoretical derivations of approximations for asymmetric bubble collapse dynamics have been done by Shima (43) and Hsieh (20). Hsieh obtained an equation governing the growth and collapse of a confocal ellipsoidal bubble. Shima found that the time of collapse increases as the ratio of R_M to the distance of the bubble centroid from the solid boundary. This conclusion was also reached by Plesset and Chapman (38) as they found the collapse time to be described by

$$\tau_c = R_M \left(\frac{\rho}{\Delta P} \right)^{1/2} \quad (51)$$

Chahine (23) found that this could also be described by

$$\tau_c = 0.915 R_{cmax} \left(\frac{\rho}{\Delta P} \right)^{1/2} \quad (52)$$

where R_{cmax} is half of the length of the major diameter of an ellipsoidal bubble.

Of particular interest concerning asymmetric collapse is the distribution of energy between production of a water jet and noise production. Mitchell and Hammitt (22) found that half of the energy from the impulse produced by the asymmetric collapse went to the jet formation and the other

half went to noise effects and viscous dissipation. They also observed that the bubbles, originally ellipsoids with the major axis parallel to the solid boundary, progressively changed shape through a spherical shape until just at collapse initiation when they were ellipsoids with the major axis normal to the solid boundary.

In one of the few instances of correlation between the produced noise spectra and dynamics of an asymmetric bubble collapse, Chanine (23) found that the noise spectrum shifts toward lower frequencies as the ratio of R_M to the centroid distance from the solid wall increases.

The conclusion to be drawn from this discussion is that the complexity of modeling nonspherical bubble collapse has inhibited its inclusion in noise production theory. For the purposes of this study, the spherical collapse assumption will be accepted.

2.2 Scaling Factors

One purpose of model testing is to find functional relationships for scaling model characteristics to full size conditions. These relationships involve powers of fluid static and bubble dynamic parameters. Experimental data is used to demonstrate the applicability of theoretically derived scaling laws. The practicality of a particular theoretical model can then be evaluated.

The parameters of greatest importance in model tests in

a water tunnel are freestream velocity and pressure. The pressure is commonly expressed in terms of cavitation number and coefficient of pressure. Of course, the dynamic pressure denominator of both of these nondimensional numbers is a function of U_∞ .

The spectral energy density predicted by incompressible theory was given by Equation (35).

$$S(f) \sim U_\infty^{2.4} R_M^{3.6} (C_p + \sigma)^{1.2} f^{-0.4} \quad (53)$$

By setting all but one parameter constant, if possible, one can find the exponential dependence of the spectral energy upon that parameter. In this case, R_M is also a function of σ which makes a direct relationship between $S(f)$ and R_M difficult to find.

The maximum in the spectrum produced by a bubble collapse in an incompressible fluid was predicted to occur at $f = 1/\tau_c$. Recalling Equation (23), this peak frequency is found to be

$$f = 0.77 \frac{U_\infty}{R_M} (C_p + \sigma)^{1/2} \quad (54)$$

Compressible theory yielded a relation for spectral energy density of

$$S(f) = \frac{(P_s \theta)^2}{1 + (2\pi\theta f)^2} \quad (55)$$

where P_s and θ are calculated by Equations (44) and (45)

respectively. For values of $P_G < 10^{-3}$ atmospheres, the Mach number term becomes insignificant in Equation (45). The role of R_M was minimized due to its logarithmic contribution. For high frequencies ($f > 1/(2\pi\theta)$), Equation (50) becomes

$$S(f) \sim R_M^2 P_G^{0.5} f^{-2} \quad (56)$$

which indicates a high frequency roll off as $1/f^2$. For this study, this roll off is above the frequency range of interest. Therefore, the approximation of Equation (50), after substitution of the results of Equations (46-49), for lower frequencies

$$S(f) \sim R_M^4 P_G \quad (57)$$

is the important result. Note that this is independent of frequency and free-stream velocity if σ is held constant in determining R_M . A relationship for P_G still needs to be found.

Blake (10) experimentally developed a functional relationship for spectral energy density of

$$S(f) \sim \tau_c \overline{P(r,t)}^2 \quad (58)$$

where $\overline{P(r,t)}^2$ is the time averaged mean square of the sound level from the collapse.

The predominant parameter in all of these functional relationships is R_M . Therefore it is necessary to develop a better understanding of the factors which determine the

maximum bubble radius such as nuclei size distribution and asymmetric collapse of the bubble.

Chapter 3

PROCEDURE

3.1 The 12 Inch Diameter Water Tunnel

This study of the bubble dynamics and resulting noise from traveling bubble cavitation was done at the Garfield Thomas Water Tunnel of the Applied Research Laboratory at The Pennsylvania State University (ARL/PSU). The primary test facility was a recirculating water tunnel with a 12 inch (0.305 m) diameter circular test section. The water velocity is continuously variable to 80 feet per second (fps)(24.4 m/s). The pressure in the test section can also be continuously controlled from 3 pounds per square inch absolute (psia)(20.7 kPa) to over 60 psia (413.7 kPa). The temperature of the water can be varied from 60° to 100° F. (15°-38° C.). The uniformity of the flow is maintained by honeycombs and filtration through 25 micron filters. A schematic of this facility is given in Figure 1.

Clear plexiglass windows were mounted on the top and two sides of the test section. The outer faces were flat while the inner faces were curved to maintain the circular cross section. The specific acoustic impedance of the plexiglass closely matches that of water which results in minimum sound reflection and maximum transmission at a water

CIRCULAR WORKING SECTION
12 IN. D. x 30 IN. LONG

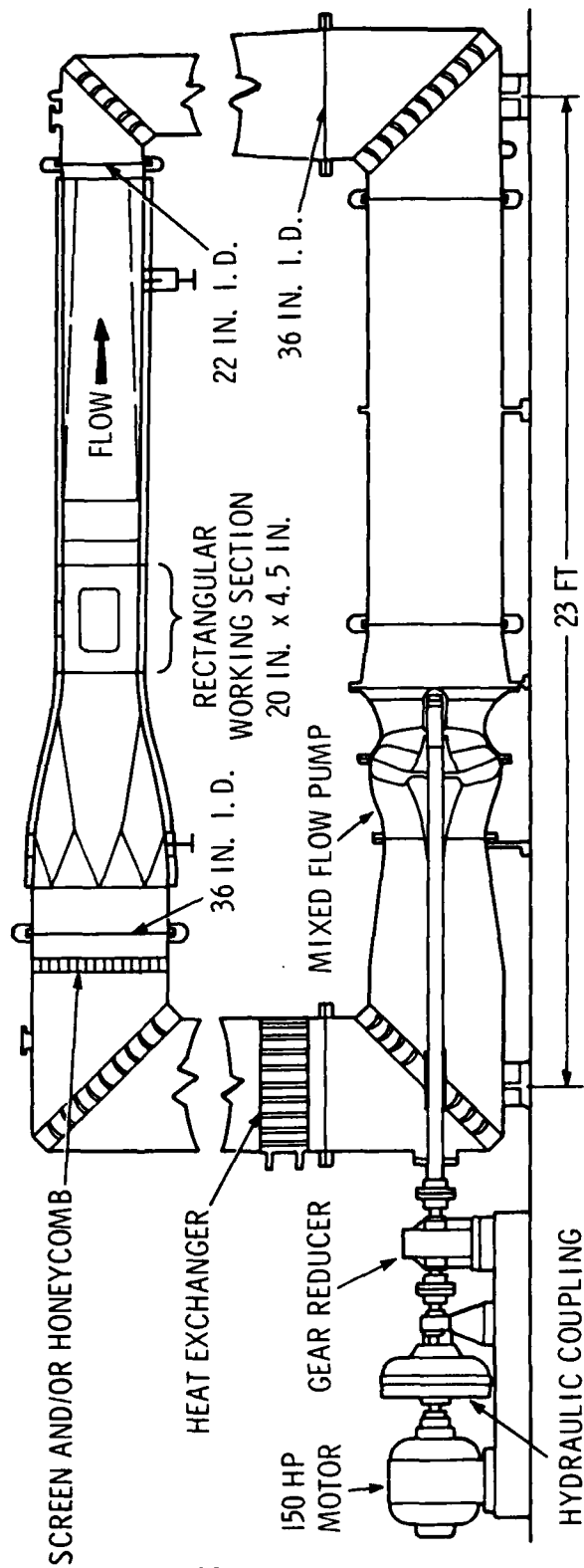
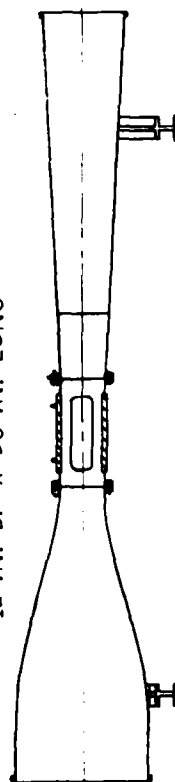


Figure 1. Illustration of the 12 Inch Diameter Water Tunnel.

and plexiglass interface. Total reflection is assumed at a water and air or plexiglass and air interface. In order to reduce the optical distortion when a laser or photographic equipment was used, one window was manufactured with a flat inner face. This window was designed so that cavitation would not be induced due to a disturbance in the flow along the wall of the circular test section.

A major objective of this study was to investigate noise characteristics at frequencies below 10 kHz. So that standing waves were not produced at desired frequencies, it was necessary to have the receiving hydrophone greater than one wavelength from the source of noise which was bubble collapse on the model body. Thus, to enable measurement down to 2.5 kHz, the hydrophone had to be situated approximately 24 inches (0.59 m) away. Since the test section has only a six inch (0.15 m) radius, a bottomless aluminum tank was attached to the top plexiglass window and filled with water to provide a hydrophone well.

3.2 Model

The model used in this study is a Schiebe body. The contour of this half body is the result of a disk source in a uniform stream. This particular body was chosen because it does not encounter laminar separation and it is most susceptible to traveling bubble cavitation (44).

The body has a maximum diameter of 2.0 inches (51 mm)

and a face diameter of 1.5 inches (38 mm). The nose is attached to a tapered afterbody which was strut mounted in the center of the circular test section. This configuration is shown in Figure 2. The actual model used was the one which Hamilton used for the majority of his tests. Wax had been used to fill mounting holes where transducers originally had been installed. The transducers were removed because they were in the near field of the noise source.

The pressure distribution along the surface of the model was measured by Hamilton (24). The local Pressure is expressed by the dimensionless quantity known as the pressure coefficient. This is defined as:

$$C_p = \frac{P - P_\infty}{\frac{1}{2} \rho U_\infty^2} \quad (59)$$

where P is the local pressure for a specific point on the model, P_∞ and U_∞ are the free stream static pressure and velocity and ρ is the mass density of the fluid medium.

A least squares polynomial curve fit was used to generate the continuous curve presented in Figure 3. The normalized length, s/a , can be correctly interpreted as inches of arc length along the model surface since the body maximum radius is one inch. The equations defining the pressure coefficient for the Schiebe body used in this study are given in Table 1.

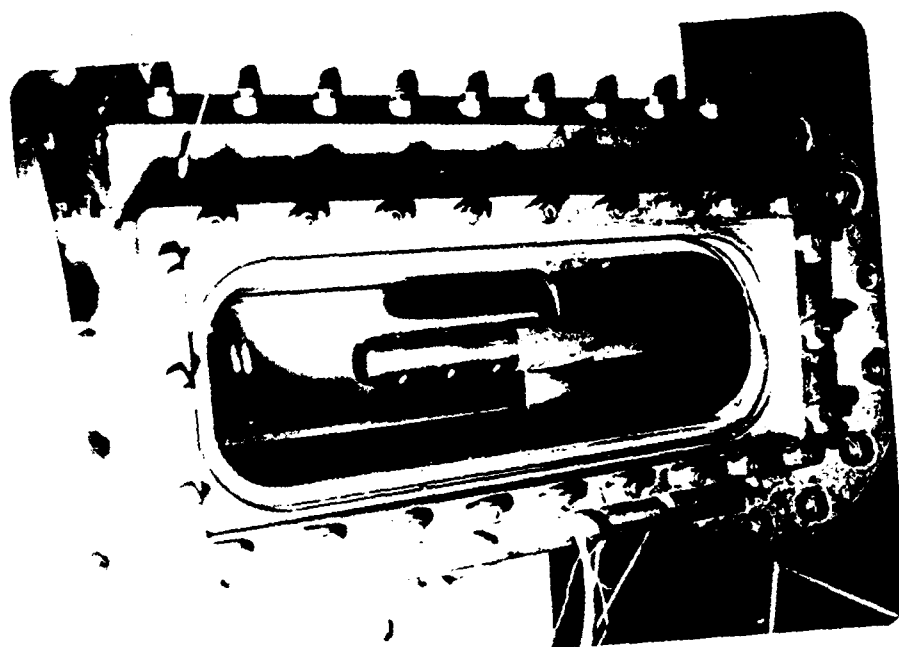


Figure 2. Schiebe Body Mounted in Test Section.

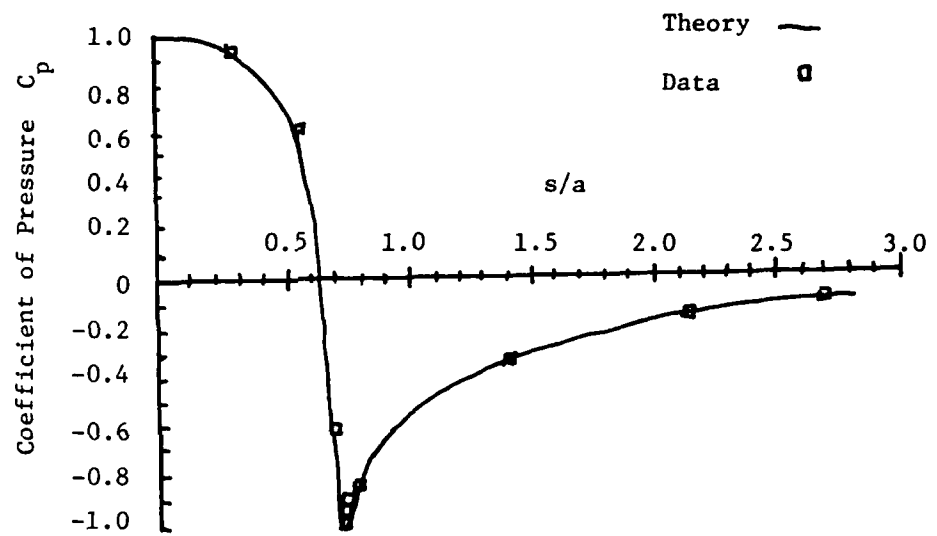


Figure 3. Interpolated Values of Coefficient of Pressure versus Surface Position on Schiebe Body.

TABLE 1
EQUATIONS DEFINING C_p ALONG
SURFACE OF SCIEBE BODY

i) $0 \leq \frac{s}{a} \leq 0.625$

$$C_p = -69.621 \left(\frac{s}{a}\right)^7 - 79.022 \left(\frac{s}{a}\right)^6 + 177.71 \left(\frac{s}{a}\right)^5 \\ - 90.038 \left(\frac{s}{a}\right)^4 + 13.037 \left(\frac{s}{a}\right)^3 + 0.085253 \left(\frac{s}{a}\right)^2 \\ - 0.25309 \left(\frac{s}{a}\right) + 1.0068$$

ii) $0.625 \leq \frac{s}{a} \leq 0.650$

$$C_p = 165.00 \left(\frac{s}{a}\right)^3 - 438.02 \left(\frac{s}{a}\right)^2 + 342.68 \left(\frac{s}{a}\right) - 83.389$$

iii) $0.650 \leq \frac{s}{a} \leq 0.745$

$$C_p = 122.46 \left(\frac{s}{a}\right)^2 - 176.80 \left(\frac{s}{a}\right) + 62.786$$

iv) $0.745 \leq \frac{s}{a} \leq 0.770$

$$C_p = 717.29 \left(\frac{s}{a}\right)^3 - 1697.7 \left(\frac{s}{a}\right)^2 + 1340.9 \left(\frac{s}{a}\right) - 354.26$$

v) $\frac{s}{a} \geq 0.770$

$$C_p = \frac{0.330}{0.390 - \left(\frac{s}{a}\right)}$$

3.3 Air Content

The total air content of the water tunnel was maintained at a relatively constant value of 10.0 parts per million (ppm) on a molar basis. This was regularly measured using a Thomas Van-Slyke blood gas apparatus. City water, used to initially fill the water tunnel, has an air content of about 17 ppm. By lowering the pressure in the tunnel below atmospheric pressure and using as low a flow velocity as possible to circulate the water, free-stream air bubbles and some other bubbles driven out of solution were removed by a vacuum pump from collecting domes on the tunnel. This was done until the air content was stabilized in the vicinity of 10.0 ppm. Since many engineering applications involve higher air contents, this investigation was done with a higher, relatively constant content of 10.5 ppm. Also, the pressure range between incipient cavitation and the development of an attached cavity is directly proportional to the air content. The relatively high air content maintained in this investigation allows a wider operating range for traveling bubble cavitation.

3.4 Measurement of Pressure and Velocity

The pressure and velocity in the test section were determined from the static and total pressures. The static pressure was obtained using a Validyne pressure transducer

comparing the pressure at a test section wall tap to atmospheric pressure.

The velocity was found from the total pressure by use of Bernoulli's equation (Eq. 2). On a streamline

$$P + 1/2 \rho U_{\infty}^2 + \rho g x_2 = \text{constant}$$

Therefore putting a stagnation probe in the same streamline at the same height gives

$$P_{\infty} + 1/2 \rho U_{\infty}^2 = P_o$$

or

$$P_o - P_{\infty} = 1/2 \rho U_{\infty}^2$$

A CEC pressure transducer was used to compare static pressure to stagnation pressure.

The outputs of both transducers was displayed on a Dymec integrating digital voltmeter. The transducers were calibrated with a piston device in a one square inch cylinder filled with water. Weights were centered on the circular disk attached to the piston and spun to reduce the effects of friction. Various weights were used to produce a range of pressures.

3.5 Measurement of Cavitation Inception and Desinence

The propensity of a particular set of flow conditions to produce cavitation is measured by the cavitation number given in Equation (16) as:

$$\sigma = \frac{P_{\infty} - P_v}{\frac{1}{2} \rho U_{\infty}^2} \quad (60)$$

where P_∞ and U_∞ are the free-stream static pressure and velocity respectively, P_v is the vapor pressure and ρ is the mass density of the liquid. For the purposes of this study, the temperature of the water was assumed to be constant thereby fixing single values for ρ and P_v . This leaves only free-stream static pressure and velocity as variable parameters.

The test matrix consisted of running a range of pressures for each of seven velocities. The velocity started with 25.0 fps (7.62 m/s) and increased in increments of 2.5 fps (.76 m/s) to an upper limit of 40.0 fps (12.20 m/s).

With the velocity set, the pressure was slowly lowered until traveling bubble cavitation was first seen with the aid of a stroboscope to freeze the motion of the bubbles. This point is cavitation inception. The static pressure is used to calculate the incipient cavitation number, σ_1 . The pressure was progressively reduced until an attached cavity formed. The cavitation number for this point was also calculated. The pressure was then raised until the traveling bubble cavitation disappeared. The pressure at this desinence point was noted for later computation of the desinent cavitation number, σ_d .

Because of the presence of free-stream bubbles at relatively high air contents and the erratic nature of the Foxboro pressure control system for the tunnel, the determination of the points of inception and desinence are

quite subjective. Hamilton tried other optical and acoustical methods of measuring cavitation but concluded that visual measuring, despite its inaccuracies, was still the preferable technique.

3.6 Noise Measurement

Noise measurements were made with a Celesco LC-10 lead zirconate titanate piezoelectric hydrophone. The hydrophone was suspended in a water filled aluminum tank mounted atop the test section, thereby allowing more accurate measurements at lower frequencies. It was directed toward the center of the Schiebe body approximately one inch downstream from the nose. This configuration is depicted in Figure 4.

The hydrophone signal was amplified and high-pass filtered at 2.5 kHz through two cascaded filters. The output was then monitored by one or more devices depending on the measurement being done.

Spectral analysis of cavitation noise was done by inputting the filtered signal to a Spectral Dynamics SD-360 real time FFT processor. Fourier transforms were done to the signal in ranges of 2.5-10kHz, 2.5-20kHz, and 2.5-100kHz. The spectra were transferred to an IBM System 7 digital computer and subsequently to an IBM System 34 digital computer. There, a hydrophone sensitivity spectrum was applied to the received spectra and then they were plotted

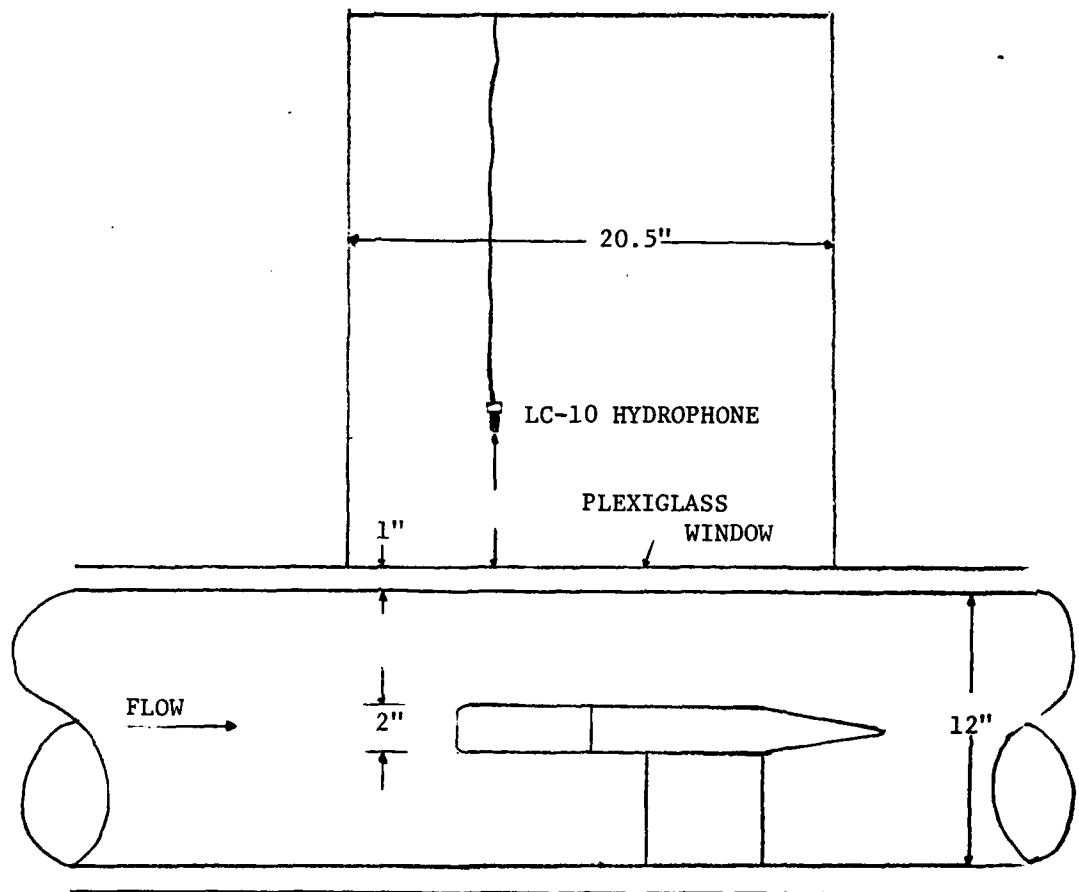


Figure 4. Configuration of Hydrophone in Water Tank
Used to Measure Cavitation Noise.

on a Calcomp model 748 flatbed plotter. Two flow velocities, 30.0 and 37.5 fps, were investigated over a range of cavitation numbers. The schematic diagram of this instrumentation is shown in Figure 5.

The sensitivity of the receiving hydrophone was established by using another LC-10 as a sound source on the surface of Schiebe body. The calibrating source was positioned approximately where cavitation bubble collapses would normally occur. This was driven with 3.0 Vrms white noise. Several spectra of the receiving hydrophone's signal were recorded for later calibration use.

Reverberation tests were also conducted with the LC-10 source. Tone bursts were used to produce a response of the receiving hydrophone which was recorded on an oscilloscope. Photographs were then taken of these responses.

An analysis of the bubble collapses per unit time and produced noise was desired to derive the noise per bubble collapse as a function of pressure. The filtered hydrophone signal was put in the SD-360, displayed, and copied for time domain analysis. Thus, collapse pulses could be recorded graphically for later counting. The filtered signal was also monitored by a true rms dB voltmeter set on a long integration time to give the produced noise level. Measurements were made over a range of cavitation numbers from traveling bubble inception to attached cavity inception for both 30.0 and 37.5 fps. The static pressure was read at

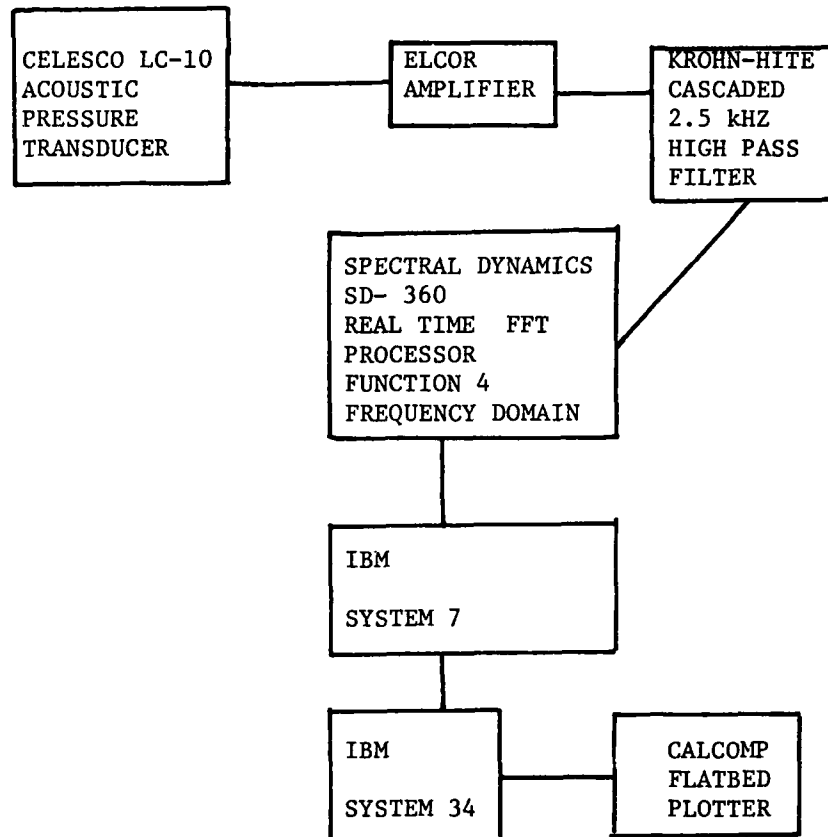


Figure 5. Schematic Diagram of Instrumentation for Cavitation Noise Spectra.

the same time that the time samples were obtained. Figure 6 shows the data acquisition system used.

3.7 Recording Bubble Dynamics

An investigation of bubble dynamics of traveling bubble cavitation and the role of K_M was done by videotaping the cavitation.

A Sony AV-3400 camera and recording system were used. The Schiebe body was backlighted with a strobe behind a diffusing screen. The best images were obtained when the bubbles were directly below the model against a light background. Images were also taken of a scale against the body for later use in dimensioning. The equipment configuration is illustrated in Figure 7.

One hour of video tape was taken for each of two flow conditions; a flow velocity of 30.0 fps and cavitation numbers of $\sigma = .80$ and $\sigma = .68$ set the conditions. While the static pressure remained relatively constant, deviations were called out for recording on the tape soundtrack.

3.8 Measurement of Gas Nuclei in Water

The role of nuclei density and size in cavitation inception has been the subject of many studies in the recent past including those by van der Walle (11), Johnson and Hsieh (45), Gates (46), Keller (14), and Gates, Billet, et.al. (15). Before the development of holographic and

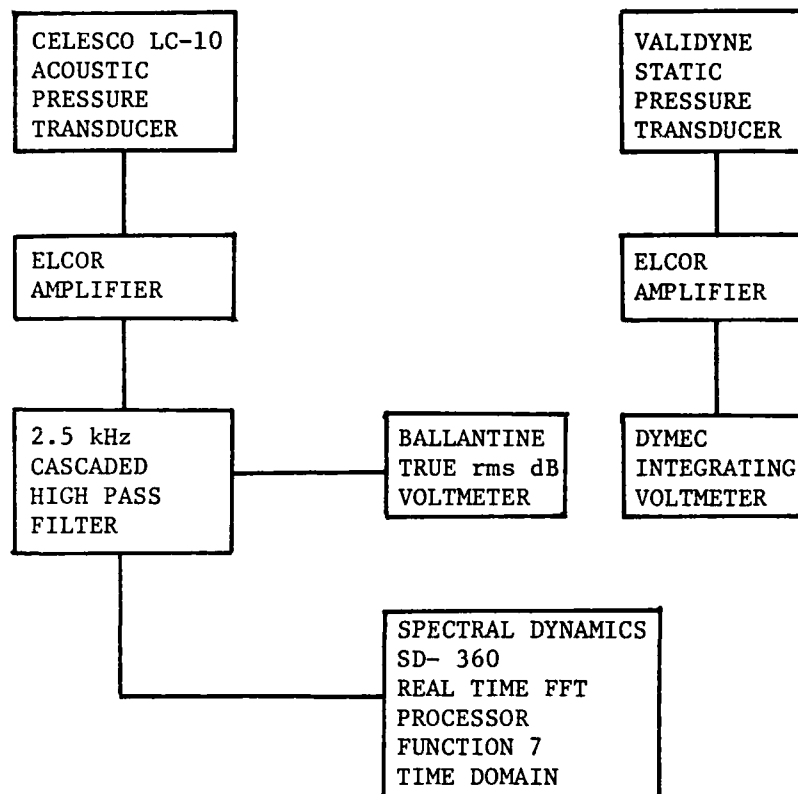


Figure 6. Schematic Diagram of Instrumentation for Cavitation Bubble Count and Noise Data.

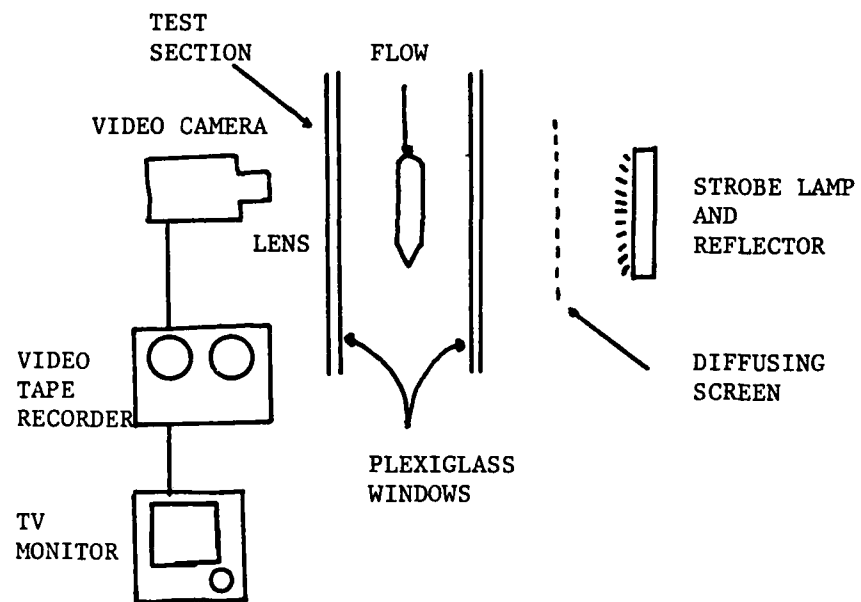


Figure 7. Schematic Drawing of Video Taping Apparatus.

light scattering systems for nuclei counting, inaccurate estimates were all that were possible. The total gas content was used as one such estimator, but one could not know the proportion of free to dissolved air let alone the nuclei size distribution. Another estimation could be derived from the attenuation of an acoustic signal across the test section. A high nuclei density results in high attenuation due to the impedance mismatch presented by the bubble surface.

One method used to determine nuclei distributions at ARL/PSU is Fraunhofer holography. A two step procedure is necessary to develop an image. First, a sample volume is illuminated with a high intensity, collimated beam of coherent, monochromatic light from a ruby laser. The interference between the coherent background and the particle-diffracted radiation exposes photographic film in the far-field of the nuclei. This Fraunhofer hologram is chemically developed and, in the second step, illuminated by another coherent beam such as that used for exposure. A three dimensional image of the test section volume is produced which can be used to count and dimension nuclei. A detailed description of the system is given in Appendix A.

This technique does have some drawbacks though. Because of the sensitivity of the laser to temperature, the intensity of the pulse at a specific setting would fluctuate. Due to the requirement of total darkness, a

wooden frame had to be constructed around the water tunnel and covered with heavy black plastic making temperature control even more difficult. This enclosure is shown in Figure 8. Therefore, several holograms needed to be taken to obtain one good enough for reconstruction. Also, the time required to count and size the particles is considerable.

But, since holography is currently the most accurate method available for obtaining nuclei distributions, it was used to obtain holograms for the two flow conditions which were video taped. The holograms were taken just previous to the commencement of taping for each condition.

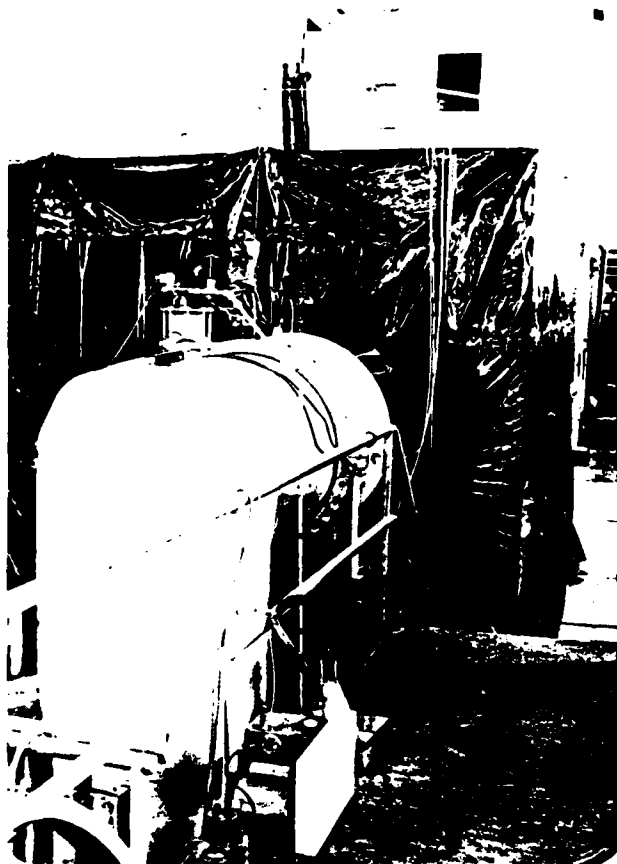


Figure 8. Enclosure for Holography.

Chapter 4

RESULTS

4.1 Cavitation Characteristics

Classical theory predicts the cavitation number for incipient and desinent vaporous cavitation to be the magnitude of the minimum pressure coefficient of the model. From the definitions of pressure coefficient and cavitation number, one finds that only if $\sigma < -C_{pmin}$ will there exist a region on the model where the local pressure is less than vapor pressure thus allowing the growth of a vaporous bubble. Therefore, $-C_{pmin}$ is used as a first approximation of the incipient cavitation number.

But cavitation does not always incept at this simply predicted value because of secondary scale effects such as model size, material, gas content of the water, and tunnel velocity. For slow tunnel speeds and high air contents, van der Walle (11) found that inception of gaseous cavitation often occurs at cavitation numbers higher than predicted. When the tunnel velocity is increased and/or the air content is lowered, the vaporous cavitation is predominant as the static pressure is lowered. It has been observed to incept at cavitation numbers below predicted.

The condition for disappearance of cavitation as the

static pressure (and therefore the cavitation number) is increased has been often found to differ from that of inception. This phenomenon is described by Holl and Treaster (47) as cavitation hysteresis.

The result of cavitation inception and desinence measurement is shown in Figure 9. Several cavitation characteristics are demonstrated by this graph. First, with $-C_{pmin}$ for the studied model equal to 1.03, the same trends are seen which van der Walle described. It is very difficult to distinguish between vaporous and gaseous cavitation when measuring inception. Secondly, desinence is shown to occur at higher cavitation numbers than inception. The degree of hysteresis or difference between inception and desinence decreases markedly with increased tunnel velocity. Also, the condition required for the inception of an attached cavity is shown to be relatively constant. Finally, characteristic cavitation numbers are proportional to the gas content.

The subjectivity of visual cavitation determination is evidenced by the maximum standard deviation. As mentioned before, efforts have been made to employ cavitation event counters. However, this method is not entirely free of human judgment as the detection threshold and the inception event rate must be chosen by someone. Gates, et. al. (15) encountered different types of cavitation and cavitation locations and subsequently discontinued use of a Keller (14) type optical event counter in favor of visual measurement.

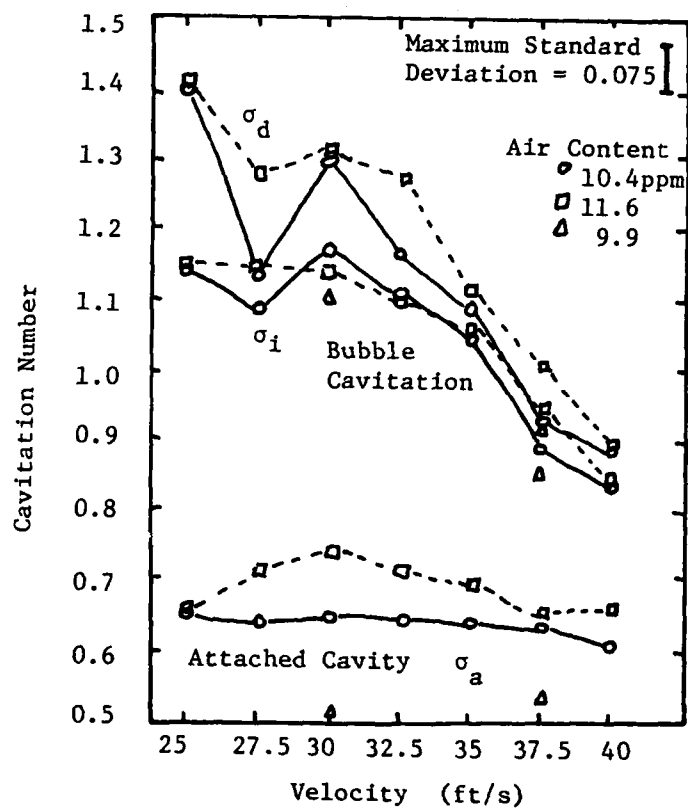


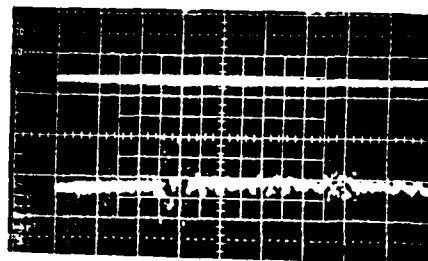
Figure 9. Cavitation Numbers for Inception and Desinence of Traveling Bubble Cavitation and Inception of an Attached Cavity as a Function of U_∞ .

4.2 Single Bubble Cavitation Noise

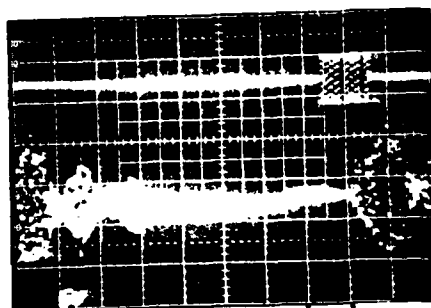
The objective of the noise tests was to obtain the far field spectrum due to a cavitation bubble collapse over the 2.5 - 100 kHz frequency range. In order to have the hydrophone at least one wavelength of the lowest desired frequency away from the source, the separation distance of the model and the hydrophone needed to be 24 inches (.59 m). But, to obtain reasonable hydrophone response in the 2.5 - 4 kHz range, the hydrophone had to be mounted 12 inches (.30 m) from the model.

Reverberation tests showed a strong signal received by direct path and indirect path reflection off of the bottom of the test section and several weaker reflections off the hydrophone tank walls. The time delay until the first response pulse was received was equivalent to the time necessary for a sound wave to travel the direct path (12"). The time until the second strong pulse was equivalent to a wave reflecting off the bottom of the test section and traveling to the hydrophone (26"). The reverberant field after shutting off a steady source showed an exponential decay with two modulations in the decay envelope. These became important in later interpretation of the bubble collapse pulses. Figure 10 shows these responses.

Bubble collapse noise bursts were recorded in the time domain for later analysis. A typical plot of a string of



(a.)



(b.)

Figure 10. Hydrophone Response to a.) 1 Cycle of a 25 kHz Sinusoid and b.) 16 Cycles of a 25 kHz Sinusoid Source Input on a Model Surface at Approximate Location of Bubble Collapse.

collapse pulses is given in Figure 11. The plots show the nulls evidenced by the reverberation tests as well as strings of closely packed collapses. These groups of noise bursts make recognition of individual pulses difficult. This is one source of possible error in obtaining the bubble collapse rate for each flow condition. Discrimination of discrete pulses is most difficult at low cavitation numbers.

The justification for modeling traveling bubble cavitation as a series of discrete bubble collapses is dependent upon the independence of collapses. As discussed in Section 2.1, a Poisson distribution of collapse events satisfies this independence criterion. The existence of this Poisson distribution can be established by the existence of an exponential distribution for the time intervals between collapses. Figure 12 shows the distribution of collapse intervals obtained from a 200 msec plot. It is indeed an exponential distribution.

With collapse independence established, the next steps toward deriving a noise per bubble relation to cavitation number were the recording of produced noise level and the counting of the cavitation pulses on the time domain records to establish collapse occurrence rates. Figure 13 is a plot of the rate of collapses versus cavitation number. The number of collapses is normalized by the body radius divided by the free-stream velocity (a/U_∞) resulting in a Strouhal number. Normally this number is associated with the

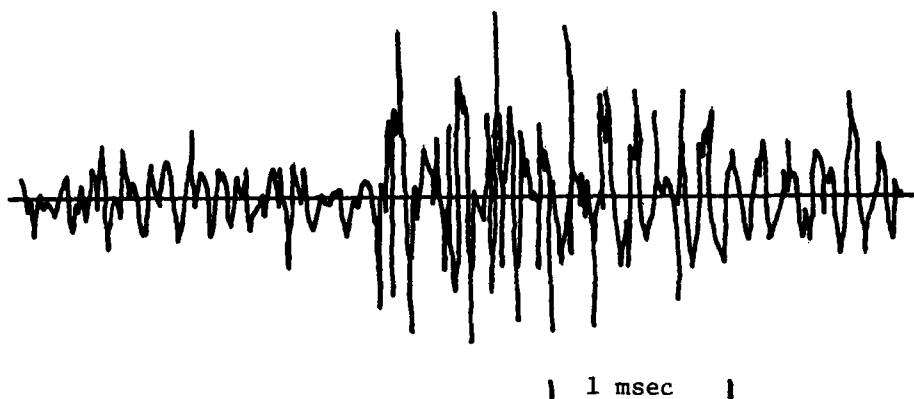


Figure 11. Example of Cavitation Noise Signal for
 $U_{\infty} = 37.5$ fps and $\sigma = .74$.

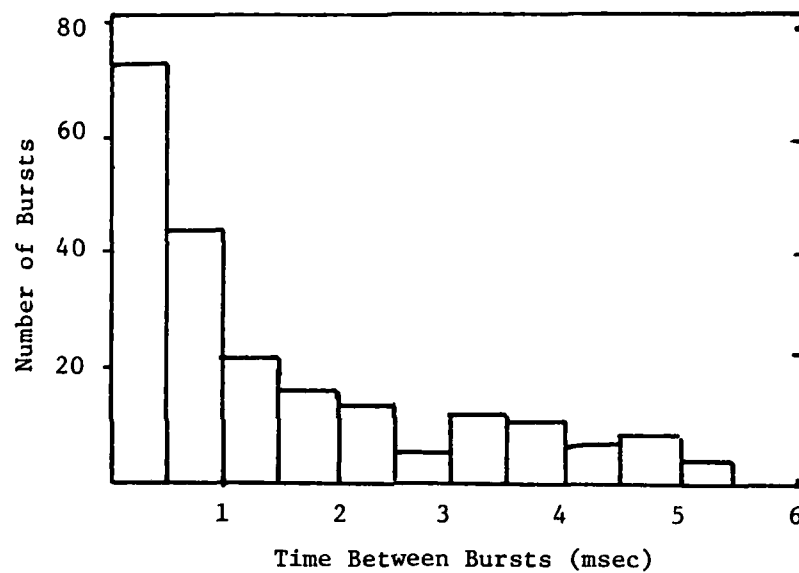


Figure 12. Noise Burst Interval Distribution

frequency of shed vortices. Here it is indicative of the frequency of another time dependent flow phenomenon - cavitation bubbles. Notice that at low cavitation numbers, the number of bubble collapses per second appears to be leveling off. This may be due in part to the difficulty in distinguishing individual collapse pulses. The collapse events are merging as the transition from traveling bubble cavitation to attached ring cavitation is approached. The overall cavitation noise level as monitored on a true rms dB voltmeter is plotted against cavitation number in Figure 14. The sound pressure was normalized by the dynamic pressure ($1/2 \rho U_{\infty}^2$) and plotted as dBrms re 1 μ Pa. The least squares fitted slopes for both Figures 13 and 14 are for the range $.67 < \sigma < .87$, which covers most of the traveling bubble cavitation range. Note also that both Figures 13 and 14 show a possible Reynolds number dependence.

Division of the total noise level by the number of bubble collapses results in the noise per bubble relation depicted in Figure 15. Because the data in Figures 13 and 14 are relatively linear on the log scales, an exponential relation of the form σ^k was assumed. The least squares obtained exponents are given in Table 2. The curve in Figure 15 was obtained by subtracting Figure 13 from Figure 14. As can be seen, these exponential values are seemingly independent of velocity. Over the measured range of σ , the data shows a $\sigma^{-2.6}$ relationship for average noise per bubble.

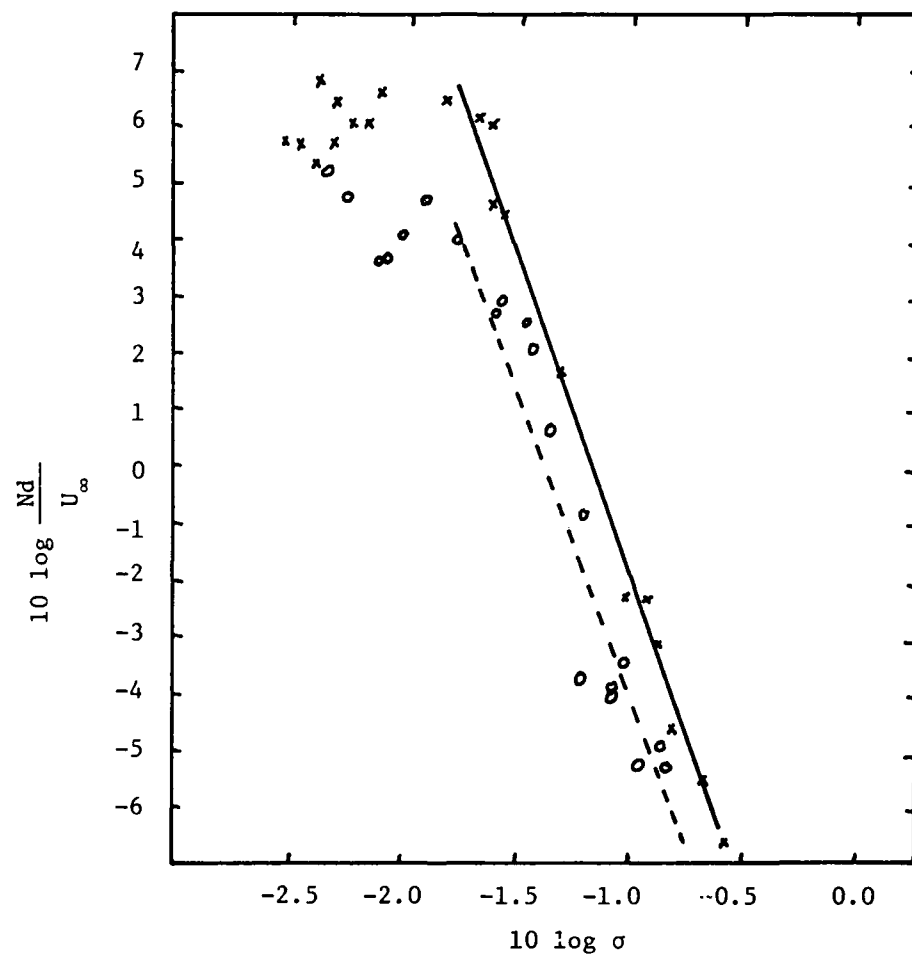


Figure 13. Nondimensional Number of Bubble Collapses per Second versus Cavitation Number for Velocities $U_\infty = 30.0$ fps and $U_\infty = 37.5$ fps.

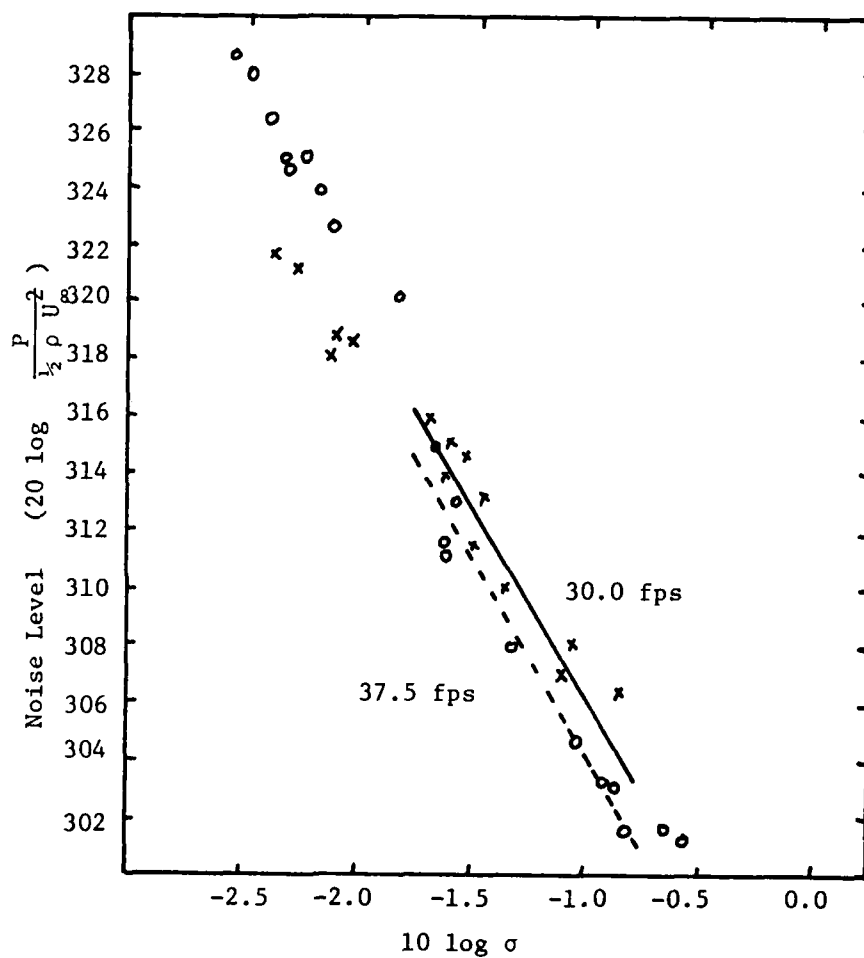


Figure 14. Nondimensional Sound Pressure Level versus Cavitation Number for Velocities $U_{\infty} = 30.0$ and $U_{\infty} = 37.5$ fps.

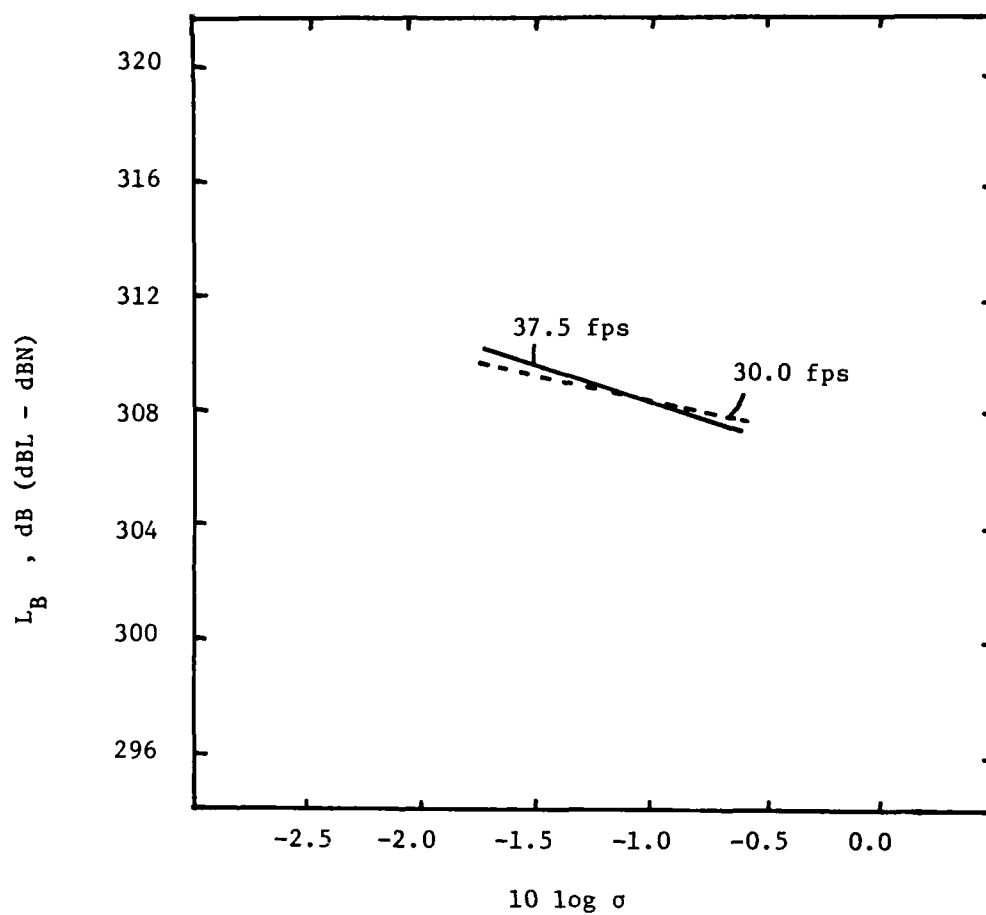


Figure 15. Cavitation Noise Level per Bubble versus Cavitation Number for Velocities of $U_\infty = 30.0$ fps and $U_\infty = 37.5$ fps.

TABLE 2

FUNCTIONAL RELATIONSHIPS FOR THE DEPENDENCE
OF N , L , L_B ON σ

Functional form σ^k assumed.

	<u>U_{∞} (fr</u>	<u>k</u>
A.) Number of Noise Bursts per Second; N	30.0	-11.23
	37.5	-11.04
B.) Noise Level; L	30.0	-13.88
	37.5	-13.58
C.) Noise Level per Bubble; L_B	30.0	- 2.65
	37.5	- 2.54

The spectrum analysis of the cavitation noise was done with a Spectral Dynamics 360 analyzer and two IBM computers. A Fourier transform was done on the signal received from the hydrophone to produce the raw spectrum. In order to derive the true energy density spectrum, the frequency response of the hydrophone must be accounted for along with the elimination of the reverberant field caused by the proximity of the tunnel walls. The procedure used to develop such a calibrated sensitivity spectrum is outlined in Appendix B. This spectrum was subtracted from the raw spectrum to yield the energy density spectrum. Low frequency noise was removed from the spectra by high pass filtering of the input signal at 2.5 kHz. The filter used has a 96 dB per octave attenuation rate below the high pass point, while above this point unity gain exists.

The resultant spectrum shows many resonances which may be due in part to calibration techniques and standing waves in the water tunnel. The calibration set-up placed the source hydrophone on the top of the model at the approximate position of bubble collapse. However, the actual collapses are distributed as a ring source around the model. The sensitivity spectrum will not remove characteristic resonances from such a distribution. Also, standing waves are present in the water tunnel which add peaks at 4860 Hz and its multiples. This same phenomenon has been encountered in other tests at this facility. The peaks are removed by an

averaging process. This technique involves drawing an envelope around the jagged spectrum as shown in Figure 16. The upper and lower values of the envelope are converted to pressure values, averaged, and changed back to a decibel value as the averaged magnitude for that frequency.

Four samples were taken for each flow condition to determine repeatability. The spectral levels were all within a four dB band. This variation is due primarily to slight differences in the cavitation numbers because of the difficulty in exactly repeating a specific tunnel pressure.

Averaged spectra for typical cavitation numbers are shown in Figures 17 and 18 for free-stream velocities of 30.0 and 37.5 fps. The frequency range is 2.5 to 80 kHz since the spectrum analyzer has an aliasing filter at the 80% spectrum point to prevent interference of high frequency and low frequency components. The low pass filter reduces the amplitudes of the high frequencies to avoid the effects of aliasing.

For higher frequencies, the spectrum is relatively level and has a weak dependence upon frequency. The spectrum seems to have reached a plateau at the higher frequencies. The higher frequency roll-off point is predicted by compressible theory but it is beyond the measured frequency range.

The absolute sound pressure levels indicated in Figures 17 and 18 are lower than expected possibly due to

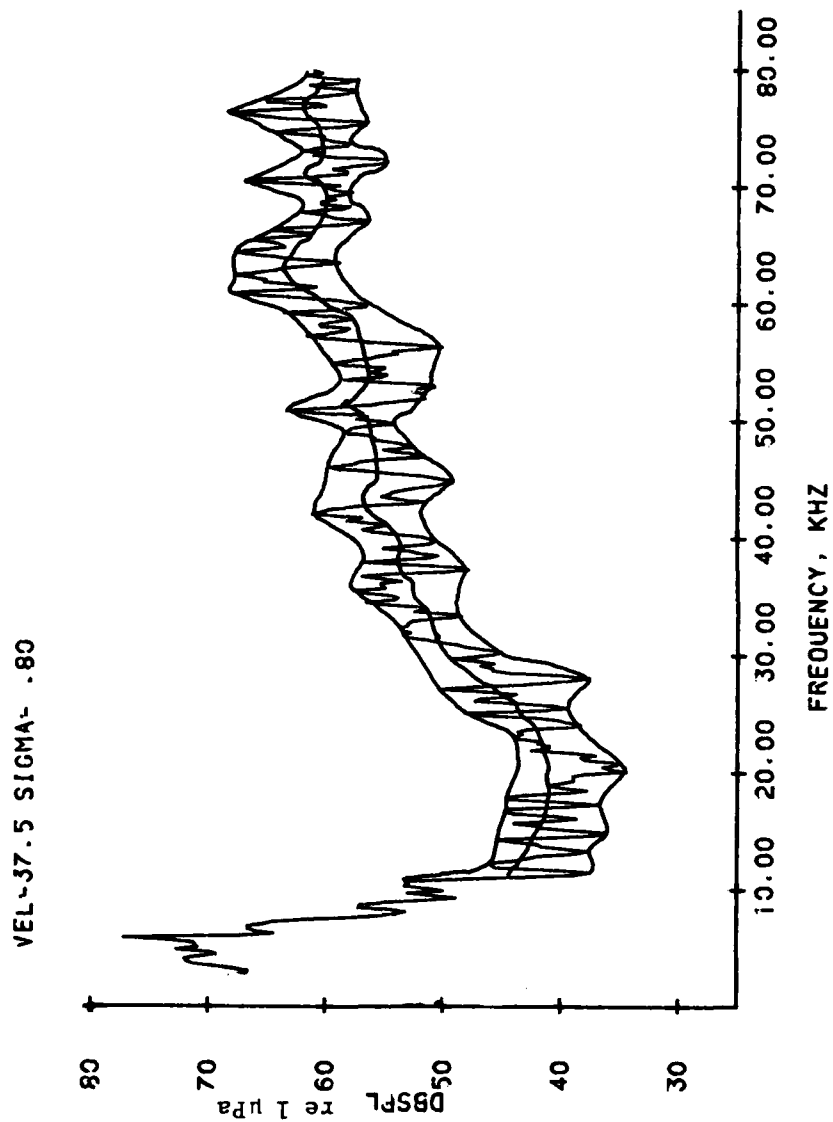


Figure 16. Spectrum Averaging Process.

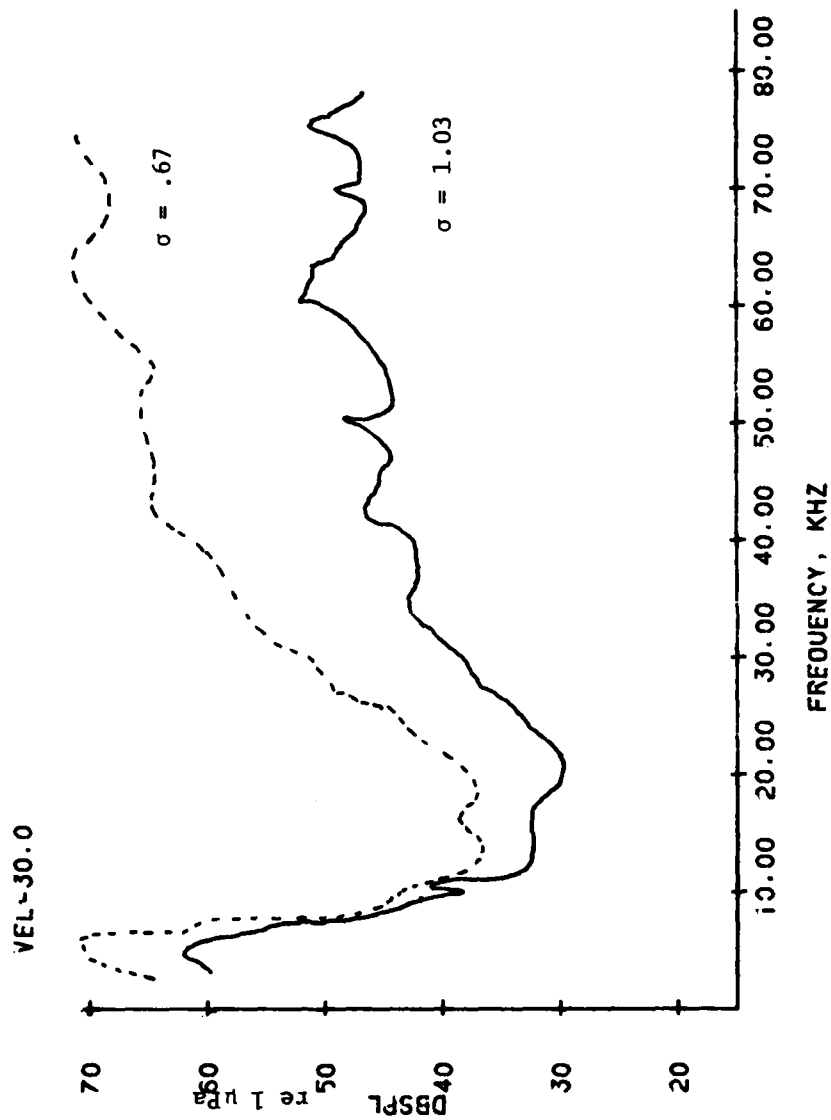


Figure 17. Averaged Traveling Bubble Cavitation 80 kHz
Noise Spectra for $U_{\infty} = 30.0$ fps.

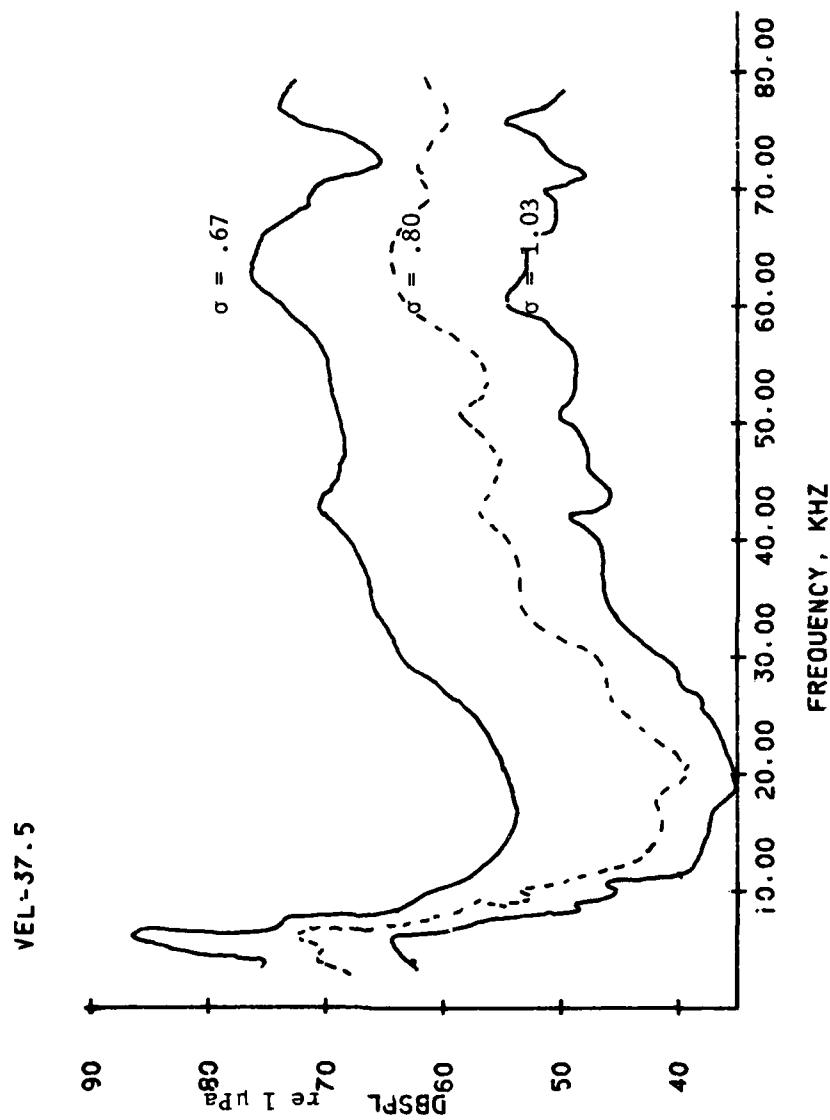


Figure 18. Averaged Traveling Bubble Cavitation 80 kHz
Noise Spectra for $U_{\infty} = 37.5$ fps.

attenuation by bubbles in the flow near the top of the test section. This condition manifested itself mostly at low cavitation numbers and especially at lower free-stream velocities.

4.3 Low Frequency Characteristics

Cavitation noise spectra were also measured over 2.5 - 10 kHz and 2.5 - 20 kHz ranges for better observation of low frequency noise. Figures 19 and 20 are typical 20 kHz spectra for the tested velocities. Once again, 80% of the spectrum is plotted because of the aliasing filter. These figures indicate a minimum difference between cavitation and background flow noise as inferred by the $\sigma = 1.03$ curves between 7 and 8 kHz. Below this frequency, there is another hump of noise energy.

Greater low frequency detail is given in Figures 21 and 22. Note that the spectrum below 2.5 kHz has been filtered out. But, it appears that there is a peak in low frequency energy at a frequency between 5 and 6 kHz which corresponds to the reciprocal of the collapse time, τ_c .

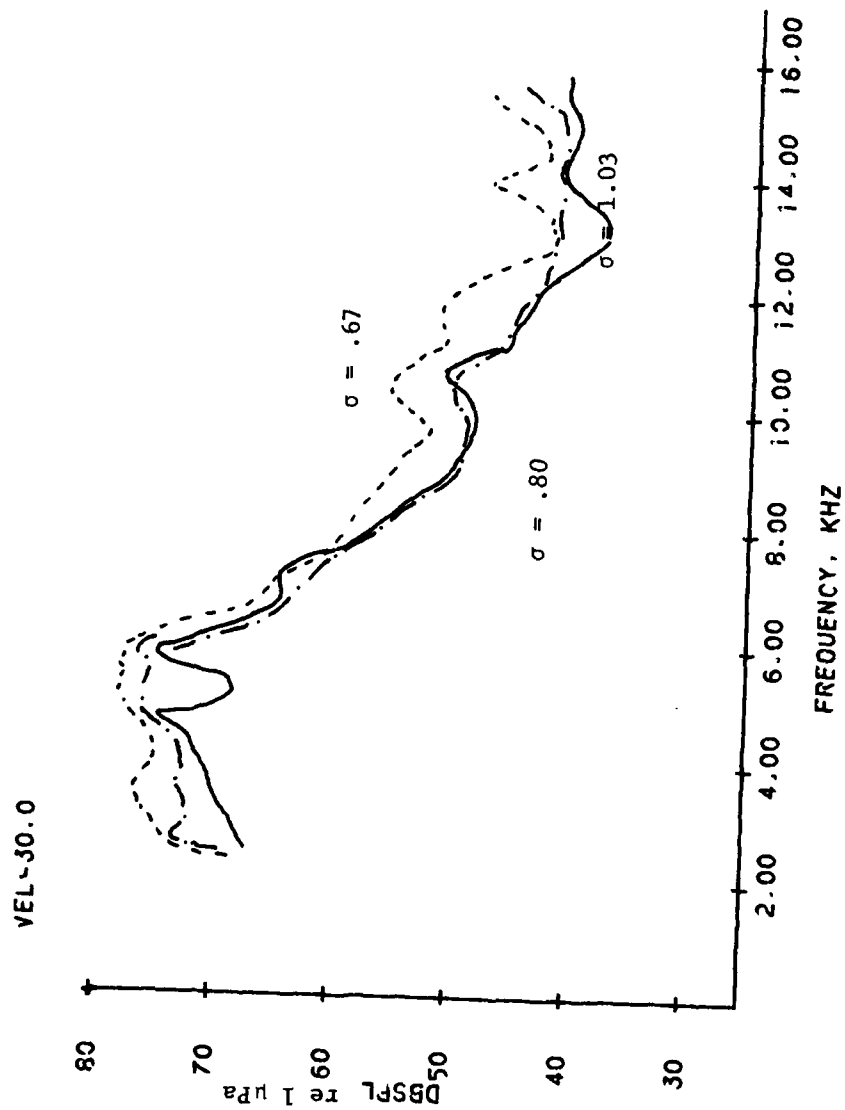


Figure 19. Averaged Traveling Bubble Cavitation 16 kHz
Noise Spectra for $U_{\infty} = 30.0$ fps.

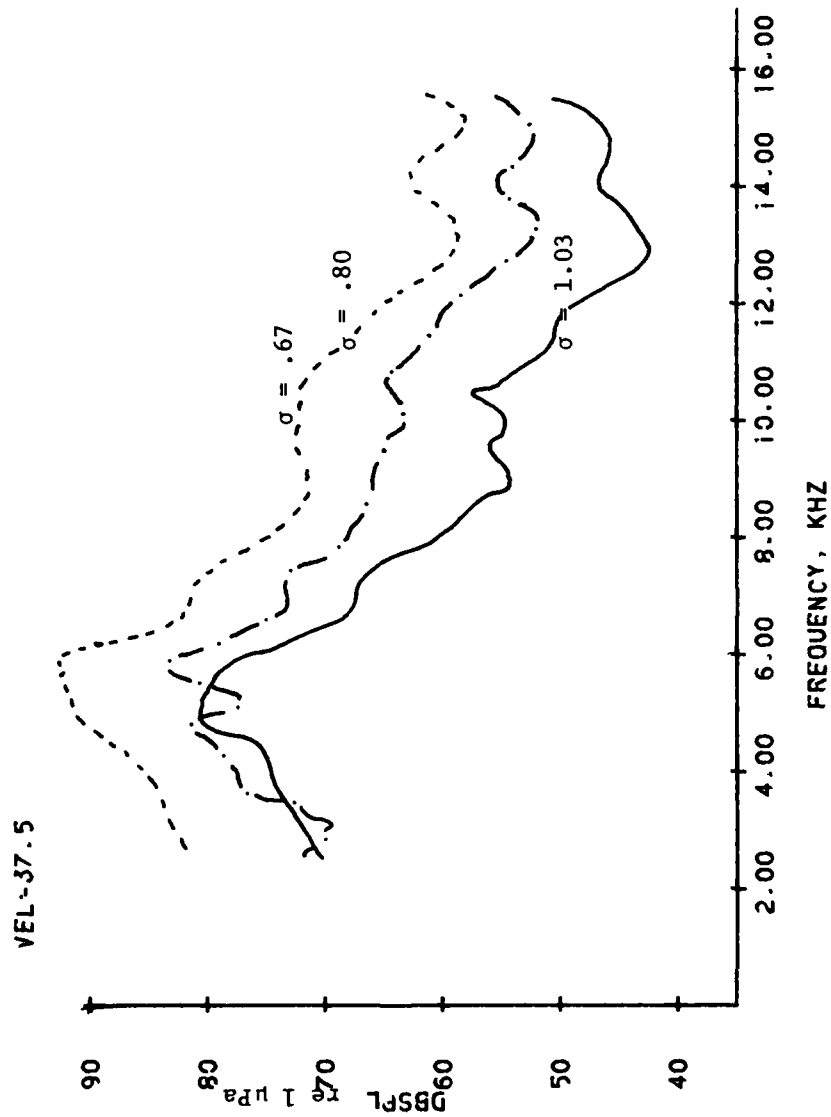


Figure 20. Averaged Traveling Bubble Cavitation 16 kHz Noise Spectra for $U_{\infty} = 37.5$ fps.

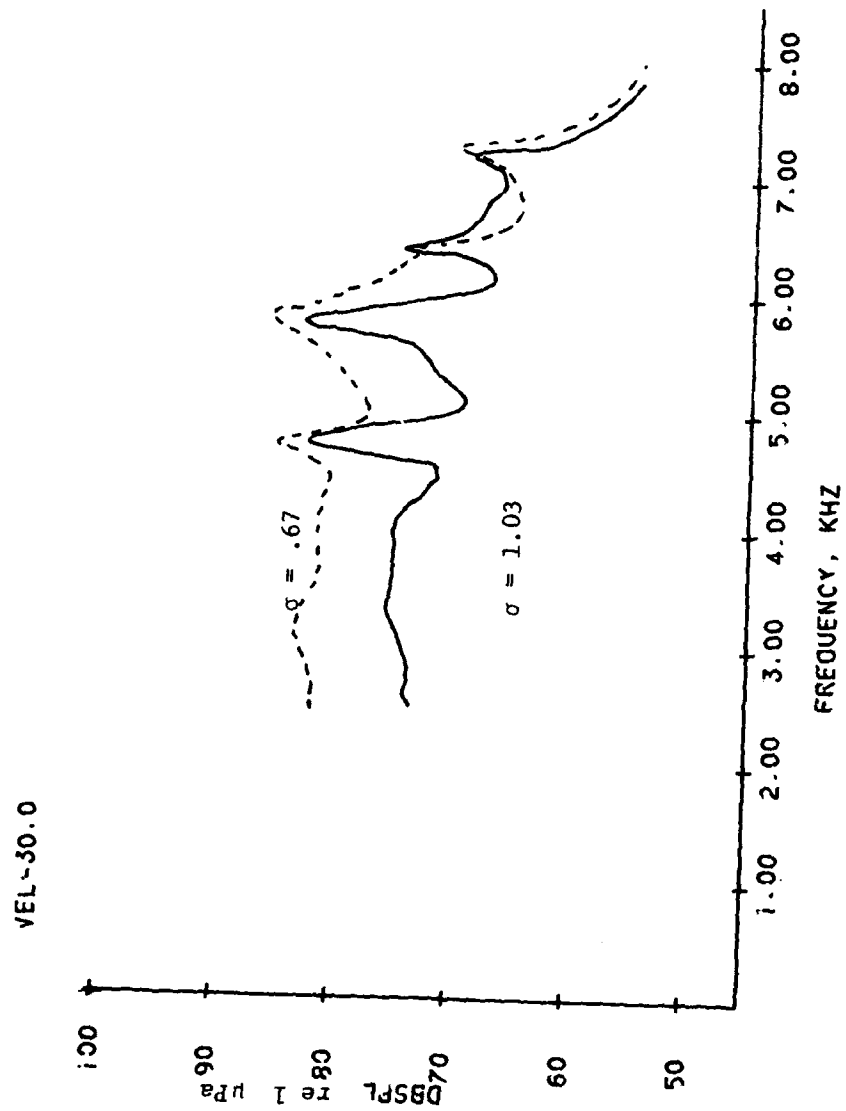


Figure 21. Averaged Traveling Bubble Cavitation 8 kHz
Noise Spectra for $U_{\infty} = 30.0$ fps.

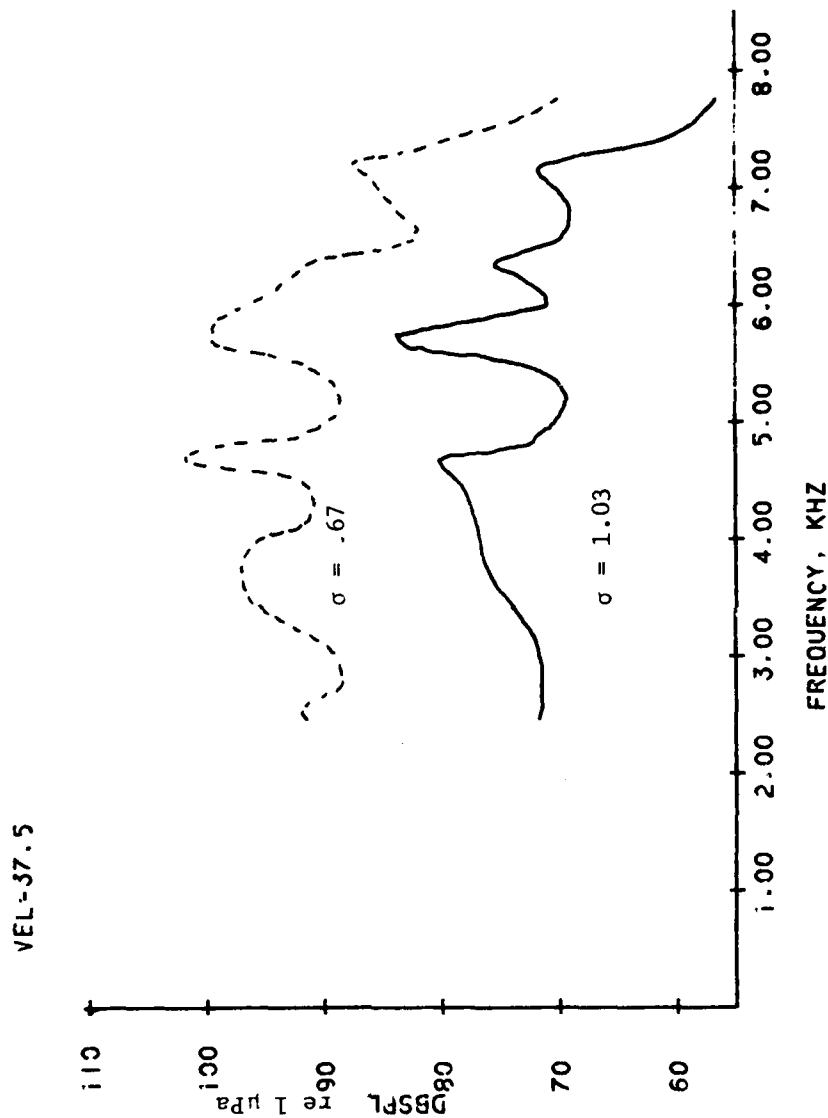


Figure 22. Averaged Traveling Bubble Cavitation 8 kHz
Noise Spectra for $U_{\infty} = 37.5$ fps.

4.4 Analysis of Bubble Dynamics

Video taping was used to record a number of cavitation bubbles distributed over the Schiebe body. Video tapes were recorded for two conditions: $\sigma = .80$ and $\sigma = .69$ with free-stream velocity of 30.0 fps. The total air content was 8.5 ppm on a molar basis.

The bubbles were measured along the backlighted profile of the model. Measurements were taken of the depth and width of the vapor bubbles as well as their positions on the body. Previous films of traveling bubble cavitation have shown the bubbles to be elliptical in profile yet circular when viewed normal to the model surface. Therefore the bubble can be considered an oblate spheroid for the purpose of calculating volume. The depth is the minor semiaxis and the width is the major axis. The bubbles tended to be flattened out at higher flow velocities.

Using the calculated volume, the radius for an equivalent volume sphere was found because the cavitation collapse is being modeled as a spherical collapse. Recall from Section 2.1.3 that Mitchell and Hammitt observed that asymmetric cavitation bubbles tended to alter in shape from the major axis parallel to the model surface to the major axis being perpendicular to the surface. Analysis of the video tapes showed a similar trend of the flattened bubbles

becoming more spherical just prior to collapse.

Because the imaging rate of a video tape system is relatively slow (about 30 images per second) only one image of each bubble was seen. Therefore a large sample of bubbles was taken by measuring size and location of each as seen on the video monitor.

The ultimate objective was to find a distribution of sizes of bubble radii at the maximum radius position on the model. The point on the model where the bubble will be at its maximum volume was determined by developing histograms of bubble sizes at several points along the model. The point associated with the histogram having the highest mean radius was assumed to be the position of R_M . Further analysis of the video tapes concentrated on the .1 inch region around that point.

The rate of occurrence of a particular bubble size was scaled from the results of the bubble size distribution for the narrow surface area on which the bubble profile could be seen. The scaling included the effect of the difference in static pressure around the body. Lower static pressure on the top of the model allowed bubbles there to grow larger than they would have on the bottom of the model.

The resultant maximum bubble radius distributions are given in Figures 23 and 24 . The average maximum bubble radius was .388 mm for the $\sigma = .80$ condition with standard deviation .194 mm. The average maximum bubble radius for the

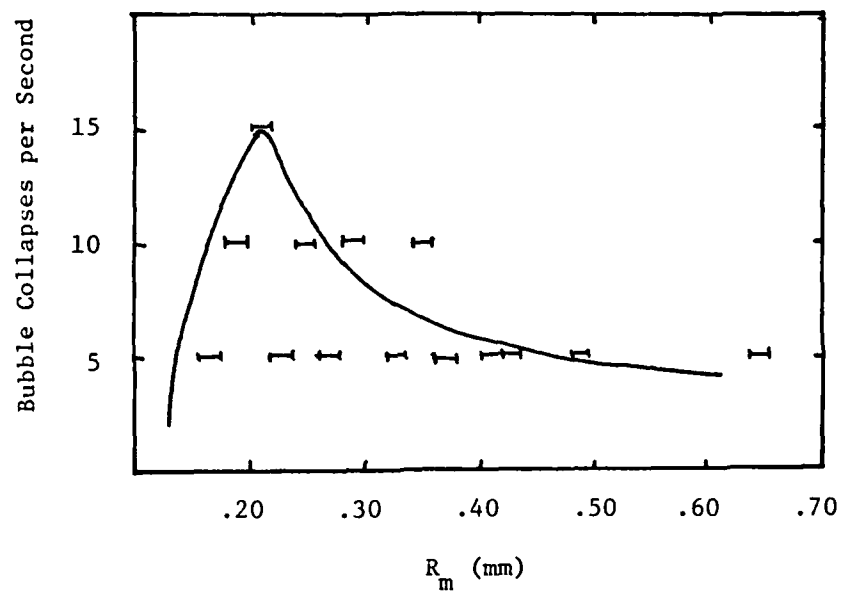


Figure 23. Maximum Cavitation Bubble Radius Distribution for $U_{\infty} = 30.0$ fps and $\sigma = .80$.

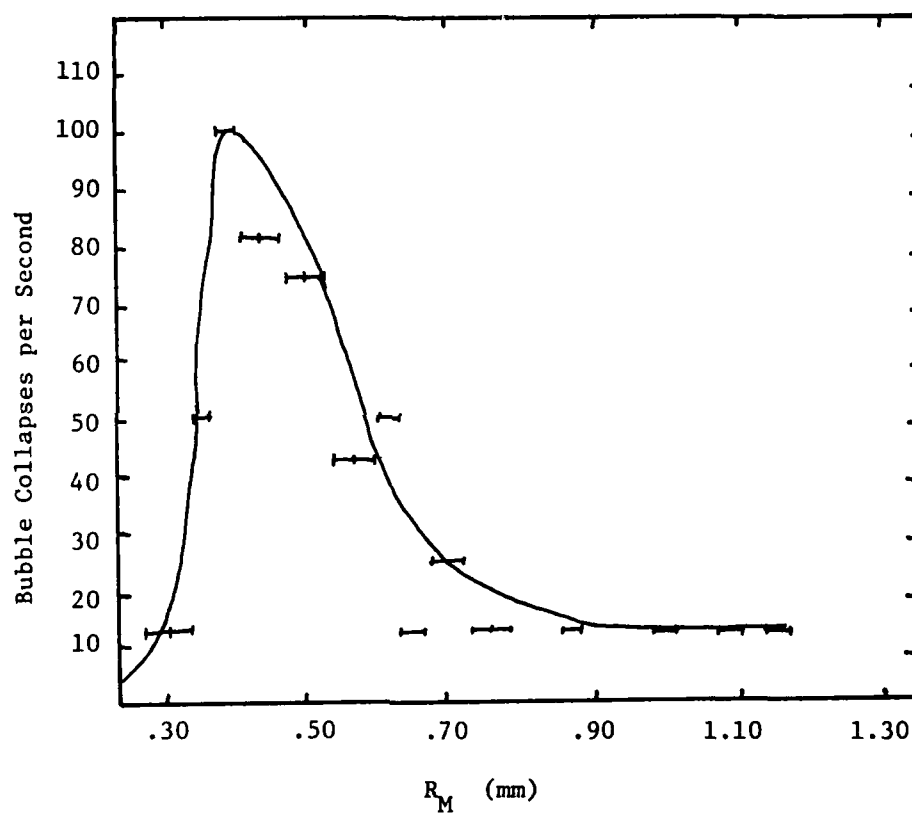


Figure 24. Maximum Cavitation Bubble Radius Distribution for $U_\infty = 30.0$ fps and $\sigma = .68$.

$\sigma = .68$ condition was .543 mm with standard deviation .194 mm. The sample size of bubbles at the point of maximum bubble radius is smaller for the $\sigma = .80$ condition than for the lower cavitation number condition. This was due to the decreased rate of cavitation events.

This technique for studying bubble dynamics is limited in that it is a statistical approach. It cannot be used to trace the growth and collapse of individual bubbles which would be necessary to investigate asymmetric collapse. The poor resolution of the TV screen ($\pm .09$ mm) also limited the accuracy of measurements.

4.5 Correlation of Bubble Dynamics to Noise Spectrum Levels

The peak pressure amplitude distribution produced by collapsing bubbles was developed from the time domain records produced by the SD 360 analyzer. The dB level above background was measured for each pulse produced by a bubble collapse. A histogram was used to collate the results. Finally, a curve fit was used to provide a smooth distribution curve. Figures 25 and 26 show the distribution of peak pressure amplitudes produced by collapsing traveling bubbles. Note that the distribution is lognormal as was the R_M distribution.

A comparison of the R_M distribution to the peak amplitude distribution yields the results in Figure 27. Equation (35) predicts a relationship of $P \sim R_M$ for bubbles collapsing far from the surface. The relationship is approximately linear. But, it cannot be known how many pressure peaks were produced by bubble rebounding nor if a particular magnitude R_M is more susceptible to rebound than another.

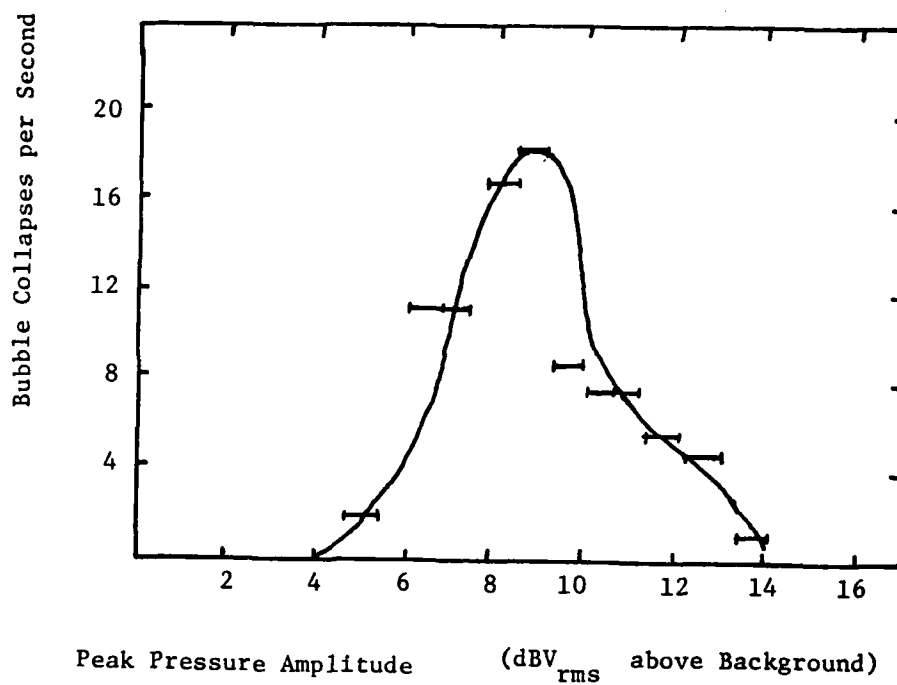


Figure 25. Cavitation Bubble Collapses per Second versus Peak Pressure Amplitude for $U_{\infty} = 30.0$ fps and $\sigma = .80$

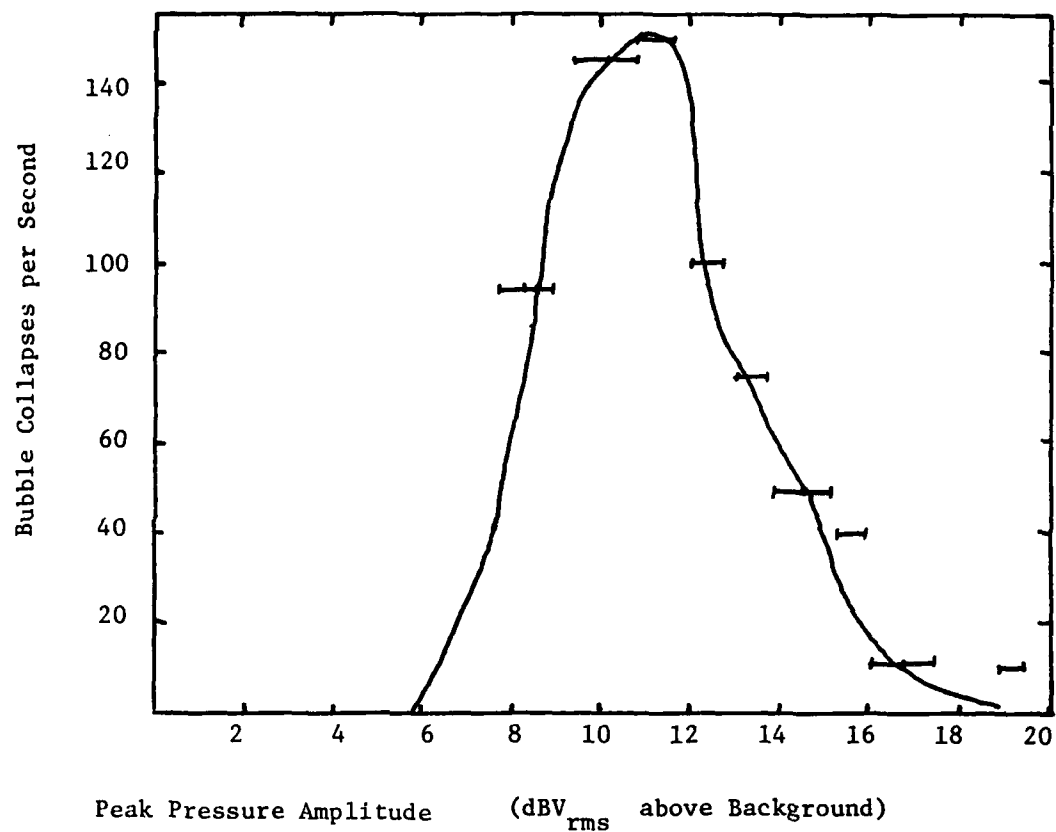


Figure 26. Cavitation Bubble Collapses per Second versus Peak Pressure Amplitude for $U_{\infty} = 30.0$ fps and $\sigma = .68$.

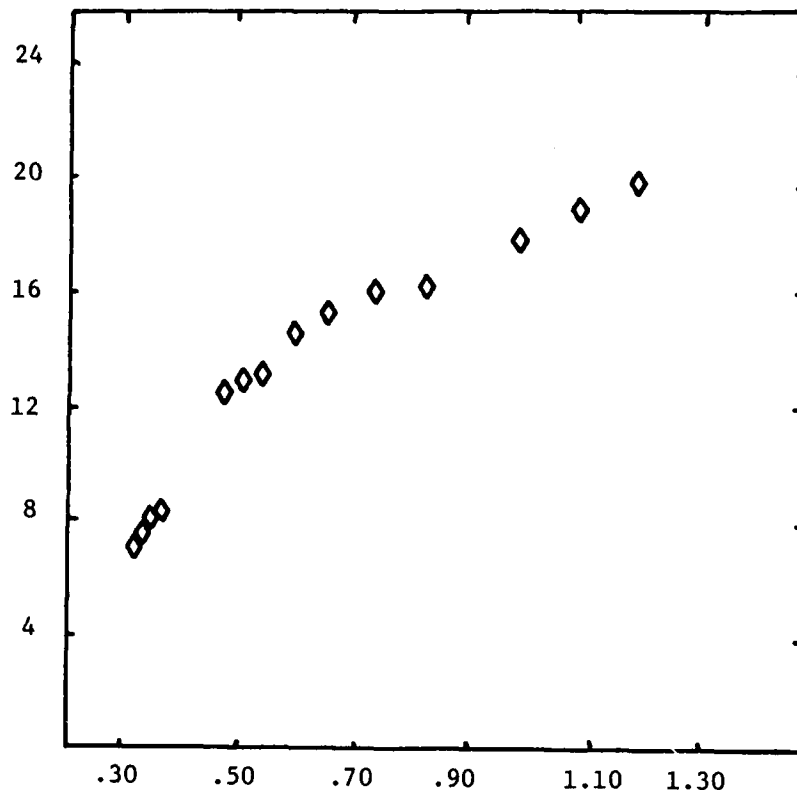


Figure 27. Peak Pressure Amplitude versus Maximum Bubble Radius for $U_{\infty} = 30.0$ fps and $\sigma = .68$.

4.6 Correlation of Bubble Dynamics to Nuclei Distribution

Nuclei distributions were holographically obtained just prior to the video taping of each of the two tested cavitation conditions. The distributions are for a volume just upstream of the Schiebe body.

The results of the analysis of the holograms are shown in Figures 28 and 29. In each case, the distribution appears to be lognormal. Oldenzien showed the form of this distribution to be

$$n_R(R) = \frac{n_0 e^{-1/2s^2}}{\sqrt{2\pi} s R_0} \exp \left[-\frac{1}{2s^2} \ln^2 \frac{R}{R_0} \right] \quad (61)$$

where s is the standard deviation and n_0 is the number of bubbles per unit volume.

The relationship of the nuclei distribution to the maximum radii distribution is not altogether clear. It may well be that the cavitation vapor bubbles grow from the average size nuclei while the small nuclei dissolve from surface tension and the large nuclei become stable gas-filled bubbles. One observation though is that a greater percentage of nuclei eventually develop into cavitation bubbles under conditions with lower cavitation numbers.

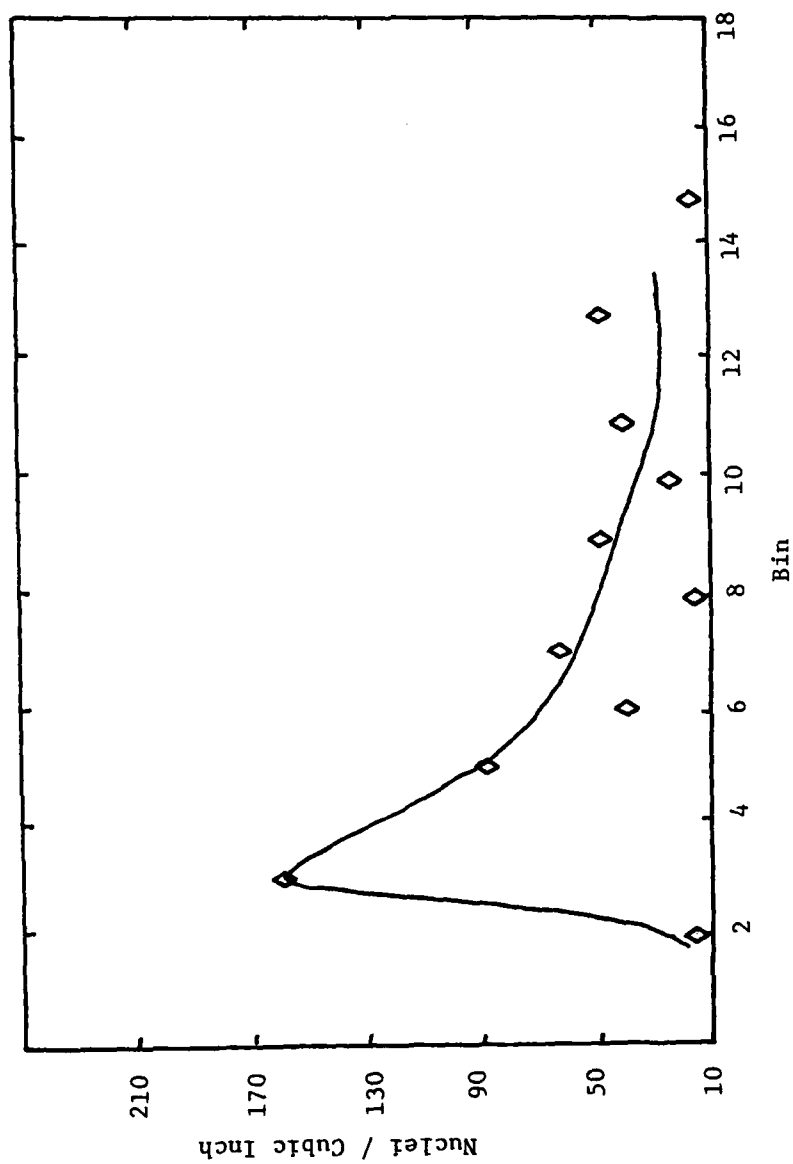


Figure 28. Nuclei Distribution for $U_{\infty} = 30.0$, $\sigma = .80$ and Total Air Content of 8.5 ppm.

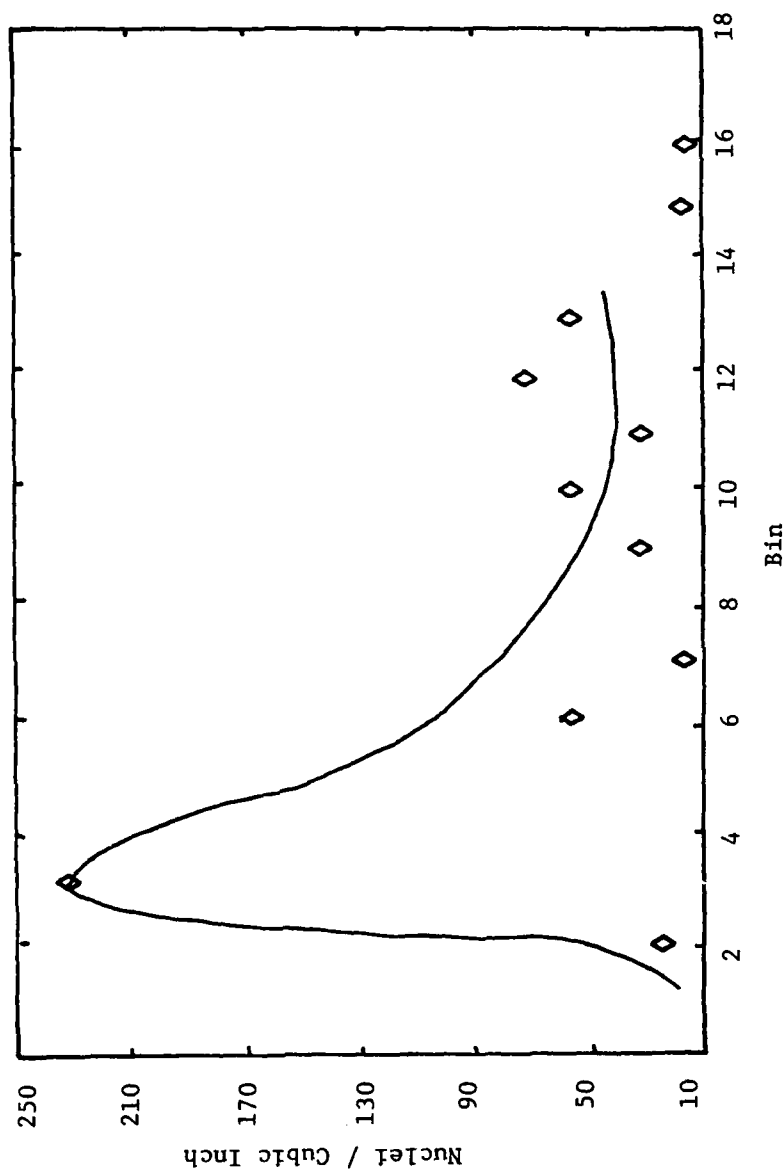


Figure 29. Nuclei Distribution for $U_{\infty} = 30.0$, $\sigma = .68$ and Total Air Content of 8.5 ppm.

TABLE 3
BIN SIZES FOR HOLOGRAPHIC NUCLEI DISTRIBUTION

<u>CHANNEL</u>	<u>BUBBLE DIAMETER (μm)</u>
0	2.0 - 4.5
1	4.5 - 7.5
2	7.5 - 10.5
3	10.5 - 14.5
4	14.5 - 18.7
5	18.7 - 24.0
6	24.0 - 31.5
7	31.5 - 40.5
8	40.5 - 52.0
9	52.0 - 68.0
10	68.0 - 86.5
11	86.5 - 123
12	123 - 195
13	195 - 281
14	281 - 467
15	467 - 726
16	726 - 1206
17	1206 - 1957

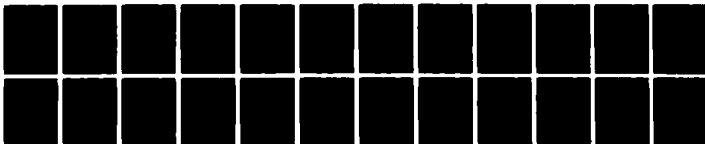
AD-A115 837

PENNSYLVANIA STATE UNIV UNIVERSITY PARK APPLIED RESE--ETC F/G 20/4
BUBBLE DYNAMICS AND RESULTING NOISE FROM TRAVELING BUBBLE CAVIT--ETC(U)
APR 82 R C MARBOE N00024-79-C-6043
ARL/PSU/TM-82-94 NL

UNCLASSIFIED

2 11 2

21 11 2



END
DATE
7 82
DTIC

Chapter 5

SUMMARY

5.1 Discussion

One of the objectives of this study was to gauge the applicability of various theories for predicting noise produced by collapsing bubbles of traveling bubble cavitation. This has taken the form of evaluation of the produced spectrum and sound pressure level.

As seen in the figures of Sections 4.2 and 4.3, the cavitation noise spectrum is composed of two portions which are modeled by different theories. The low frequency portion is described by incompressible theory. There is a peak in the spectral energy density at an approximate frequency determined by the reciprocal of the collapse time, τ_c . The presence of a solid boundary results in asymmetric collapse of the bubbles which shifts this peak to $1/(1.5\tau_c)$. The latter frequency was observed by both Blake (10) and Ross (1). This is also approximately equivalent to Chahine's findings given by Equation (52). Blake and Gibson (41) also found this relationship. Calculating the collapse time from Equation (25) and using $1/(1.5\tau_c)$ to find the peak, the frequency found for $U_\infty = 30.0$ fps and $\sigma = .68$ was 4.9 kHz. Similarly for $U_\infty = 37.5$ fps and $\sigma = .68$, the peak frequency

derived was 6.1 kHz. When these values are compared to the peaks in Figures 19 and 20, a close correspondence can be seen. The values of t_c derived were on the order of .1 msec for the Rayleigh equation and .14 msec for the Gilmore equation but the time domain records show a t_c of closer to .18 to .20 msec to be more accurate. It is reasonable though to expect $1/t_c$ to overpredict the peak frequency because its derivation is based upon the assumption of a void cavity collapsing symmetrically. The presence of a permanent gas in the bubble will retard the wall motion resulting in a longer collapse time.

This low frequency spectral shape has been observed by many investigators including Mellen (8), Fitzpatrick and Strasberg (9), and Barker (48). This portion of the spectrum extends to approximately the frequency determined by the reciprocal of the combined growth and collapse time of the bubble reaching a minimum.

Above that point, the spectrum rises until reaching a plateau which covers most of the 10 - 100 kHz range. This can be seen in Figures 17 and 18. This level spectrum is indicative of a shock wave. Compressible theory is best suited for this portion of the spectrum. Hamilton (24), Blake, and Barker all found a similar level spectral shape for this higher frequency range. Lauterborn and Timm (49) even observed two shock waves produced by one asymmetric collapse. A high end roll-off point is predicted by

compressible theory, but the measured frequency ranges do not extend that high.

Since incompressible theory is applicable until the final stages of collapse, it is interesting to compare the noise level per bubble results of this study to the levels predicted by incompressible theory.

Substitution of the maximum bubble radius relation of Equation (20) into the incompressible prediction for spectral energy density given by Equation (53) yields the following dependence upon σ :

$$S \sim (\overline{C_p} + \sigma)^{9/5} (C_p' + \sigma)^{6/5} \quad (62)$$

where $\overline{C_p}$ is the average coefficient of pressure in the $P < P_v$ region and C_p' is the local coefficient of pressure initiating collapse. As an estimate of $\overline{C_p}$, it is reasonable to use C_{pmin} giving $\overline{C_p} = -1$. Using the results shown in Figure 3 and the video tape results for point of collapse initiation, a value of $C_p' = -.33$ was found. When these values are incorporated into Equation (60), it becomes

$$S \sim (1 - \sigma)^{9/5} (\sigma - .33)^{6/5} \quad (63)$$

This is plotted in Figure 30. Also plotted are the experimentally derived functional relationships found by this study ($\sigma^{-2.6}$) and Hamilton ($\sigma^{-8.4}$). Note that each is a reasonable approximation to the curve over the cavitation ranges tested. This suggests that incompressible theory can

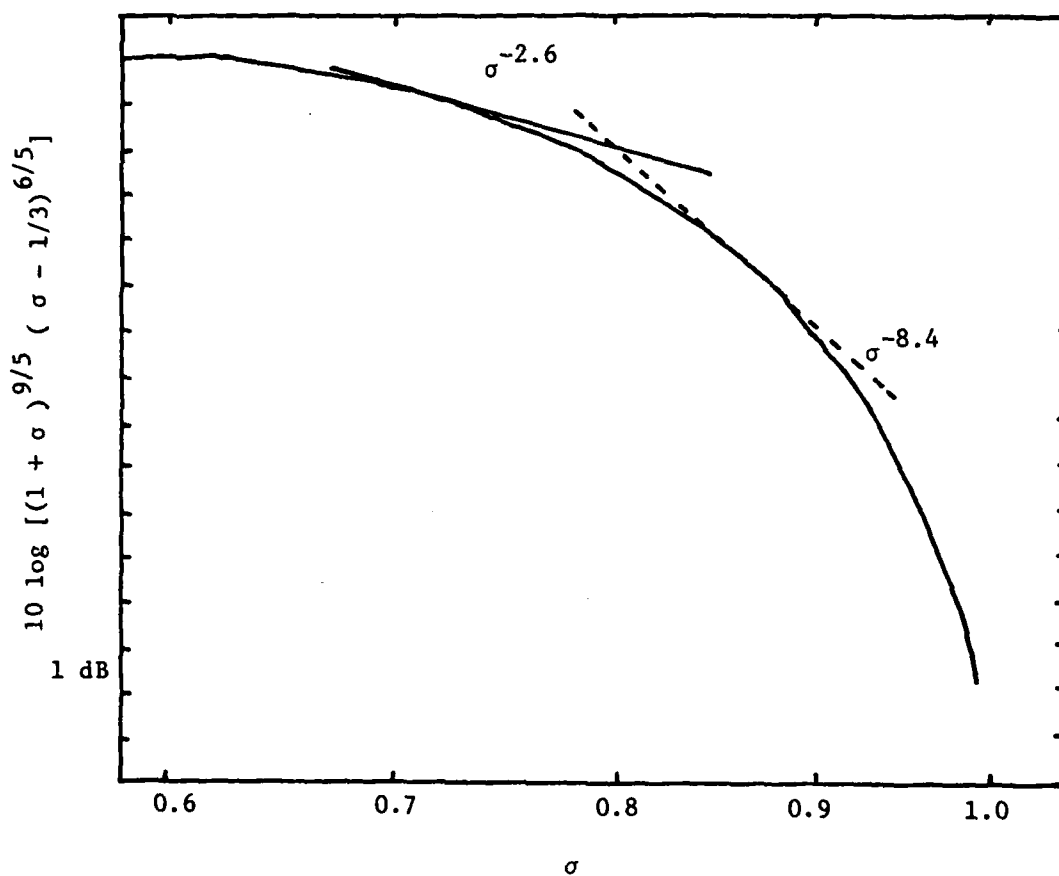


Figure 30. Comparison of Experimental Results of Hamilton (24) and Present Study to Incompressible Theory for Traveling Bubble Cavitation.

model the spectral energy.

The absolute sound pressure levels are lower than expected due to high frequency attenuation by bubbles near the top of the test section. Another contributing factor suggested by Chahine (23) is the directivity of noise produced by the collapse of a bubble near a solid boundary. He found that noise is radiated normal to the surface and attenuated in directions parallel to the surface. This is possibly due to the presence of many small bubbles resulting from the bubble collapse. The cylindrical body used in this study would tend to reflect Chahine's findings because of the distribution of bubble collapses around the body. Jones and Edwards (50) found a peak pressure of 320 dB re 1 μ Pa for bubble collapse. This is about 10 dB higher than the level indicated in Figure 15.

The relationship between the nuclei distribution, the maximum bubble radius distribution, and the peak pressure amplitude distribution is a progressive one. All of these distributions were found to have a lognormal shape. The linear relationship between the peak pressure amplitude and maximum bubble radius contrasts that found by Chahine of

$$P \sim .7 \tau^{2.5} \quad (64)$$

where τ is substituted due to its linear dependence on R_M . It should be realized however that Chahine's results were for bubbles collapsing far from a solid boundary.

The one parameter which occurs in all of the noise prediction theories that is the most difficult to determine is the maximum bubble radius. Several relations have been found to predict R_M . Equation (20) predicts R_M for $U_\infty = 30.0$ fps and $\sigma = .80$ and $.68$ to be $.364$ mm and $.939$ mm respectively. Blake et. al. found the relationship

$$R_M = \left[\frac{U_\infty^2}{2} (-\sigma - C_{pmin}) \right] \frac{d}{U_\infty (1 - C_p)} \quad (65)$$

for traveling bubbles on a solid surface. This yields $.115$ mm and $.446$ mm for the respective flow conditions. The results of video tape analysis were $.388$ mm and $.543$ mm for the two cavitation conditions tested.

The lower latter two sets of numbers may be the result of the influence of a solid boundary on bubble growth. Therefore it is necessary to investigate the dynamics of growth further in order to develop a more accurate prediction of R_M .

5.2 Conclusions

This study has examined the relation of bubble dynamics to the noise produced by traveling bubble cavitation. The spectral shape and sound pressure levels have been used to evaluate the ability of theories derived for the collapse of single bubbles to describe well developed traveling bubble cavitation.

The conclusions to be drawn from the study can be summarized as follows.

- * For frequencies greater than approximately 10 kHz, the spectral energy density is a very weak function of frequency indicative of a shock wave. Compressible theory best describes this portion of the spectrum.
- * For frequencies below 10 kHz, the spectral energy density is a function of frequency with a peak at $1/\tau_c$. This is indicative of the noise produced by bubble collapse in an incompressible liquid. Incompressible theory is better suited for this lower frequency range.
- * The magnitude of $1/\tau_c$ is overpredicted by incompressible theory due to the presence of a permanent gas in the cavitation bubble.
- * Asymmetric bubble collapse may be responsible for the shift of the spectrum toward lower frequencies than predicted by theories derived for spherical bubble collapse.
- * The experimentally derived dependence of noise level per bubble collapse of $L \sim \sigma^{-2.6}$ is a close approximation to the relation
$$S \sim (\bar{C}_p + \sigma)^{9/5} (\sigma + C_p')^{6/5}$$
over the range $.67 < \sigma < .84$.
- * The amplitude distribution of peak pressure produced by a collapsing bubble, the maximum bubble radius distribution, and the nuclei distribution are all lognormal.

This study has touched on several areas which require further investigation. The effects of asymmetric bubble collapse upon noise production is important to most practical applications of noise scaling. The dependence of the maximum bubble radius distribution upon the free-stream velocity and cavitation number is needed since R_M plays such

an important role in theoretical noise predictions. Also, the high frequency roll-off is another area to be studied. One further recommendation for followup is to establish the exponential dependence of the spectral energy density upon the cavitation number over other ranges of σ . With the peak pressure amplitudes from the time domain plots, a follow-on project could model the cavitation noise process as a Poisson distribution of Dirac delta functions of variable amplitude and obtain the autocorrelation and then the spectrum as described by Rice (28).

REFERENCES

1. Ross, D., Mechanics of Underwater Noise, Pergamon Press New York, 1976.
2. Bessant, W.H., Hydrostatics and Hydrodynamics, Art. 158, Cambridge University Press, London, 1859.
3. Rayleigh, Lord (Strutt, J.W.), "On the Pressure Developed in a Liquid During the Collapse of a Spherical Cavity," Philosophical Magazine, 39, 94-98, August, 1917.
4. Gilmore, F.R., "The Growth and Collapse of a Spherical Bubble in a Viscous Compressible Liquid," California Institute of Technology, Report 26-4, 1952.
5. Mellen, R.H., "Spectral Pressure Waves of Finite Amplitude from Collapsing Cavities," U.S. Navy Underwater Sound Laboratory, New London, CT, Report 326, 1956.
6. Bahl, S.K. and Ray, J., "Collapse and Expansion of a Gas Bubble in a Liquid Subject to a Surface Tension," Soviet Physics-Acoustics, 18, 391-393, 1972.
7. Willard, G.W., "Ultrasonically Induced Cavitation in Water: A Step-by-Step Process," J. Acous. Soc. Amer., 25, 669-686, 1953.
8. Mellen, R.H., "Ultrasonic Spectrum of Cavitation Noise in Water," J. Acous. Soc. Amer., 26, 356-360, May, 1954.
9. Fitzpatrick, H.M. and Strasberg, M., "Hydrodynamic Sources of Sound," First Symposium on Naval Hydrodynamics, Publication 515, September, 1956.
10. Blake, W.K., Wolpert, M.J., Geib, F.E., and Wong, H.T., "Effects of Boundary-Layer Development on Cavitation Noise and Inception on a Hydrofoil," David W. Taylor Naval Ship Research and Development Center, Report 76-0051, December, 1976.

11. van der Walle, F., "On the Growth of Nuclei and the Related Scaling Factors in Cavitation Inception," Proc. Fourth Symposium on Naval Hydrodynamics, O.N.R. ACR-92, 357-404, 1962.
12. Apfel, R.E., "The Role of Impurities in Cavitation Threshold Determination," J. Acous. Soc. Amer., 48, 1179-1186, 1970.
13. Lauterborn, W., "Photographic Study of Tensile Strength of Water Using a Centrifuge," Acustica, 22, 35-47, 1969.
14. Keller, A.P., "The Influence of the Cavitating Nucleus on Cavitation Inception, Investigated with a Light Counting Method," J. Basic Eng., 917-925, 1972.
15. Cates, E.M., Billet, M.L., Katz, J., Doi, K., Holl, J.W. and Acosta, A.J., "Cavitation Inception and Nuclei Distributions - Joint ARL/CIT Experiments," California Institute of Technology, Report E244.1, September, 1979.
16. Oldenziel, D.M., "Bubble Cavitation in Relation to Liquid Quality," Delft Hydraulics Laboratory, Netherlands, Publication no. 211, 1979.
17. Hickling, R. and Plesset, M.S., "Collapse and Rebound of a Spherical Bubble in Water," Physics of Fluids, 7, 7-14, 1969.
18. Morozov, V.P., "Cavitation Noise as a Train of Sound Pulses Generated at Random Times," Soviet Physics-Acoustics, 14, 361-365, 1969.
19. Plesset, M.S. and Chapman, R.B., "Collapse of an Initially Spherical Vapour Cavity in the Neighborhood of a Solid Boundary," J. Fluid Mechanics, 47, 283-290, 1971.
20. Hsieh, D-Y, "On the Dynamics of Nonspherical Bubbles," J. Basic Eng., 94D, 655-665, 1972.
21. Kozirev, S.P., "On Cumulative Collapse of Cavitation Cavities," J. Basic Eng., 90D, 116-124, 1968.
22. Mitchell, T.M. and Hammitt, F.G., "Asymmetric Cavitation Bubble Collapse," J. Fluids Eng., 95, 29-37, 1973.

23. Chahine, G.L., Courbiere, P., and Carnaud, P.,
"Correlation Between Noise and Dynamics of
Cavitation Bubbles," Sixth Conference on Fluid
Machinery, Budapest, 17-22 September, 1979.
24. Hamilton, M.F., "Travelling Bubble Cavitation and
Resulting Noise," Applied Research Laboratory,
Pennsylvania State University, Technical Memorandum
81-76, 1981.
25. Levkovski, Yu.L., "Statistical Characteristics of Bubble
Cavitation," Soviet Physics-Acoustics, 19, 135-138,
1973.
26. Choi, S.C., Introductory Applied Statistics in Science,
Prentice-Hall, Englewood Cliffs, NJ, 1978.
27. Akulichev V.A. and Ol'shevskii, V.V., "Relationship
Between the Statistical Characteristics of Acoustic
and Cavitation Noise," Soviet Physics-Acoustics,
14, 22-26, 1968.
28. Rice, S.O., "Mathematical Analysis of Random Noise,"
Selected Papers on Noise and Stochastic Processes,
Wax, N., ed., Dover, New York, 1954.
29. Pierce, A.D., Acoustics: An Introduction to Its Physical
Principles and Applications, McGraw-Hill, New York,
183-189, 1981.
30. Baiter, J.J., "Aspects of Cavitation Noise," Proc. of
Symposium on High Powered Propulsion of Ships,
Wageningen, The Netherlands, December, 1974.
31. Noltingk, B.E. and Neppiras, E.A., "Cavitation Produced
by Ultrasonics," Proc. Phys. Soc. London, 638,
674-685, 1950.
32. Flynn, H.G., "Physics of Acoustic Cavitation in Liquids,"
Physical Acoustics Principles and Methods, Vol. 1
part B, Mason, W.P., ed., Academic Press, New York,
57-172, 1964.
33. Flynn, H.G., "Cavitation Dynamics: IV. Collapse of
Transient Cavities," University of Rochester,
Acoustical Physics Laboratory, 28 July, 1978.
34. Cramer, E., "The Dynamics and Acoustic Emission of
Bubbles Driven by a Sound Field," Cavitation and
Inhomogeneities in Underwater Acoustics, Lauterborn,
W., ed., Springer-Verlag, Berlin, 1980.

35. Esipov, I.B. and Naugol'nykh, K.A., "Collapse of a Bubble in a Compressible Liquid," Soviet Physics-Acoustics 19, 187-188, 1973.
36. Flynn, H.G., "Cavitation Dynamics: III. Thresholds and the Generation of Transient Cavities," University of Rochester, Acoustical Physics Laboratory, 25 July, 1978.
37. Benjamin, T.B., In Second Symposium on Naval Hydrodynamics, O.N.R. ACR-33, 207-229, 1958.
38. Shutler, N. and Mesler, R.A., "Photographic Study of Dynamics and Damage Capabilities of Bubbles Collapsing Near Solid Boundaries," J. Basic Eng., 87D, 2, 511-517, 1965.
39. Benjamin, T.B. and Ellis, A.T., "The Collapse of Cavitation Bubbles and the Pressures Thereby Produced Against Solid Boundaries," Phil. Trans. Royal Soc., London, A, 260, 221-240, 1966.
40. Plesset, M.S., "The Dynamics of Cavitation Bubbles," J. Applied Mechanics, 16, Transactions of ASME, 71, 277-282, 1949.
41. Blake, J.R. and Gibson, D.C., "Growth and Collapse of a Vapour Cavity Near a Free Surface," J. Fluid Mechanics, 111, 123-140, 1981.
42. Lauterborn, W. and Bolle, H., "Experimental Investigations of Cavitation Bubble Collapse in the Neighbourhood of a Solid Boundary," J. Fluid Mechanics, 72, 391-399, 1975.
43. Shima, A., "The Behavior of a Spherical Bubble in the Vicinity of a Solid Wall," J. Basic Eng., 90, 75-89, 1968.
44. Schiebe, F.R., "Measurement of the Cavitation Susceptibility of Water Using Standard Bodies," St. Anthony Falls Hydraulic Laboratory, University of Minnesota, Report 118, February, 1972.
45. Johnson, V.E. and Hsieh, T., "The Influence of the Trajectories of Gas Nuclei on Cavitation Inception," Proc. Sixth Symposium on Naval Hydrodynamics, O.N.R. ACR-136, 163-182, 1966.

46. Gates, E.M., "The Influence of Freestream Turbulence, Freestream Nuclei Populations and a Drag-reducing Polymer on Cavitation Inception on Two Axisymmetric Bodies," California Institute of Technology, Eng. Report No. 183-2, 1977.
47. Holl, J.W. and Treaster, A.L., "Cavitation Hysteresis," J. Basic Engin., 88D, 199-212, 1966.
48. Barker, S.J., "Measurements of Radiated Noise in the Caltech High-Speed Water Tunnel - Part II: Radiated Noise from Cavitating Hydrofoils," Graduate Aeronautical Laboratories, California Institute of Technology, March, 1975.
49. Lauterborn, W. and Timm, R., "Bubble Collapse Studies at a Million Frames Per Second," Cavitation and Inhomogeneities in Underwater Acoustics, W. Lauterborn, ed., Springer-Verlag: Berlin, 1980.
50. Jones, I.R. and Edwards, D.H., "Forces Generated by Collapse of Transient Cavities," J. Fluid Mechanics, 7, 596-609, 1960.
51. Gates, E.M. and Bacon, J., "A Note on the Determination of Cavitation Nuclei Distributions by Holography," Jour. of Ship Research, 22 no. 1, 29-31, March, 1978.

APPENDIX A

FRAUNHOFER HOLOGRAPHY

The far field or Fraunhofer diffraction pattern of particles in the water tunnel test section is photographically captured by illumination of a sample volume by a collimated beam of coherent, monochromatic light. The developed photographic plate is called a hologram.

In the reconstruction process, the hologram is illuminated by a collimated beam of coherent, monochromatic light again. A three dimensional image of the desired volume is produced for visual inspection for sizing and counting particles.

Gates and Bacon (51) have used a holographic system very much like that used at ARL/PSU. They have obtained very accurate results for nuclei distributions using this system.

The following is an adaptation of their description of the system (51).

A.1 Holocamera

The holocamera combines a light source, a beam-expander and a photographic plate to produce a hologram. A detailed illustration is given by Figure A1. Because the particles are small and moving at high velocities, the exposure time

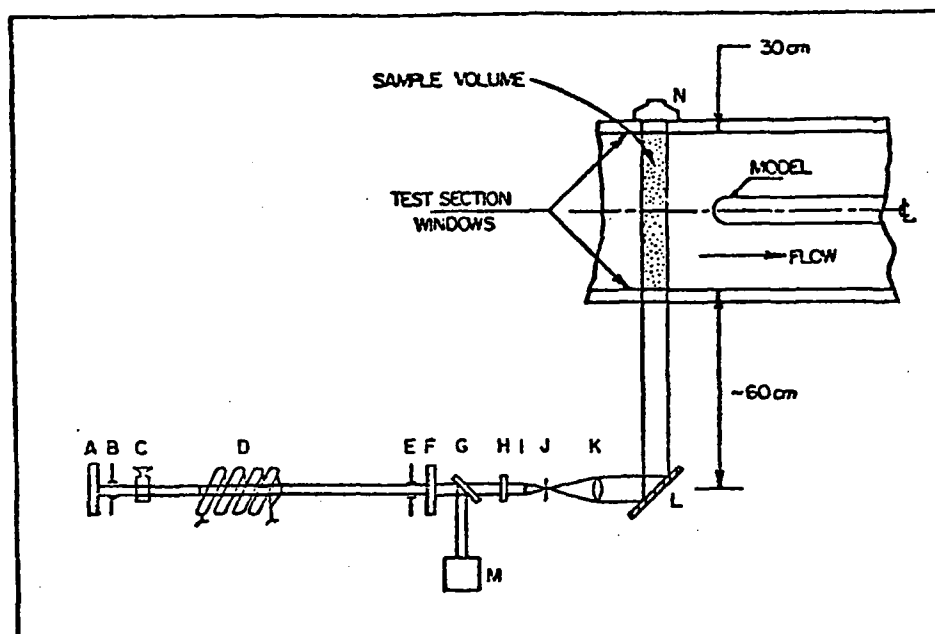


Fig. A1 Schematic drawing of holocamera: (A) dielectric mirror; (B) iris; (C) spectrophotometer cell; (D) ruby rod-flashlamp assembly; (E) iris; (F) dielectric mirror; (G) beamsplitter; (H) neutral density filter; (I) 1.6-cm focal length lens; (J) 25- μ pinhole; (K) 43.2-cm focal length collimating lens; (L) front surface mirror; (M) pin diode; (N) filmholder (51)

must be short in order to freeze the motion. Consequently, a high intensity light such as that available from a Q-switched, ruby laser is necessary.

The ruby rod in the laser is pumped by a helical xenon flashlamp. This assembly is located between two flat, dielectric mirrors. The optical duct formed has an iris near each mirror; the apertures of which can be set to reduce the number of modes of the laser output. A spectrophotometer cell inside the optical cavity contains a saturable dye called cryptocyanine in acetone solvent. In a procedure called Q-switching, the concentration of cryptocyanine is increased allowing a reduction of the laser output to a single 20 nanosecond pulse.

The laser output passes through a beam expander composed of a roughly 1.6 cm focal length lens which expands the beam, a pinhole in its focal plane of approximately 25 microns to eliminate irregularities and a 45 cm focal length lens to collimate the expanding beam. A front surface mirror redirects the beam 90 degrees. The beam then passes through the water tunnel test section and exposes a photographic plate held against the test section window. A neutral density filter before the beam expander controls the film exposure.

A.2 Reconstruction System

For reconstruction of the test volume, the chemically

developed hologram is illuminated by another laser beam through a similar combination of expanding lens, pinhole, and collimating lens. The hologram is mounted on an XYZ vernier carriage along the axis of the beam. The reconstructed particles are imaged through a microscope onto a vidicon and displayed on a large close circuit video screen. Particles are sized off the screen. Figure A2 shows the reconstruction system.

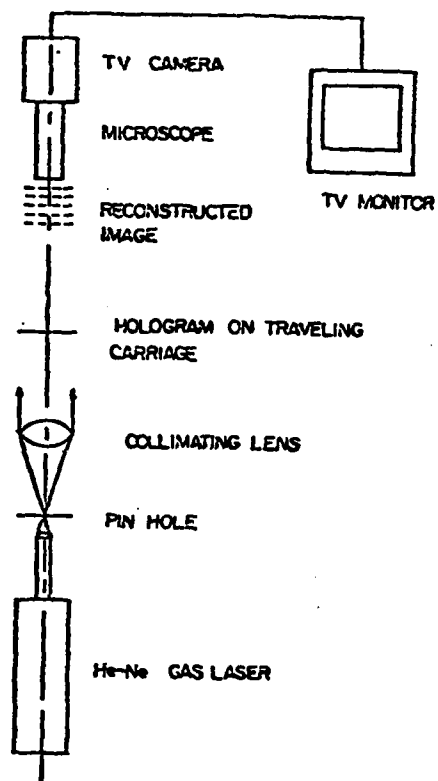


Figure A2. Schematic Drawing of Reconstruction and Viewing System. (51)

APPENDIX B

DATA ACQUISITION SYSTEM SENSITIVITY APPLICATION TO ACOUSTIC SPECTRA

In order to obtain the actual spectrum of cavitation noise, a hydrophone response spectrum had to be considerably manipulated.

A receiver hydrophone response spectrum was changed from dBV levels referenced to 0.1 volt to a cavitation noise spectrum by application of a so called sensitivity spectrum. This spectrum consisted of several correction factors which are included in Equation B1 to derive a corrective decibel level for each frequency band.

$$\text{dBsens} = \text{dBv} - \text{dBcal} - \text{dBx} + \text{dBd} - \text{dBm} \quad (\text{B1})$$

where dBv is the spectral level of the receiving hydrophone response, dBcal is the sound source strength per volt input, dBx is the voltage input to the sound source, dBd is a correction for the separation distance from the source to the receiver, and dBm is a correction for inherent machine attenuation.

The distance factor is given by:

$$\text{dBd} = 20 \log (x / 1 \text{ meter}) + \text{dB re } 1 \text{ m.} \quad (\text{B2})$$

The input voltage magnitude correction is obtained from:

$$\text{dBx} = 20 \log (V/ 1 \text{ volt}), \text{ dB re 1 volt rms} \quad (\text{B3})$$

The spectral analyzer had an inherent amount of attenuation through its electronic hardware. This varied from day to day but was on the order of 6 dBV.

When all of these factors are summed to obtain a sensitivity spectrum, the decibel level is in dB re volt rms per uPa. In order to obtain the correct final decibel levels in dB re 1 μPa , some corrections had to be made also to the spectra from the receiving hydrophone after spectral analysis. The corrections are given by Equation B4.

$$\text{dB}_r = \text{dB}_h - \text{dB}_{\text{gain}} + \text{dB}_{\text{atten}} + \text{dB}_{\text{bandwidth}} \quad (\text{B4})$$

where dB_r is the corrected received spectrum in dB re 1 volt corrected by 3 dB from peak to peak to rms, dB_h is the filtered receiver input to the spectrum analyzer, dB_{gain} is the amount of gain used to amplify the signal, dB_{atten} is the amount of attenuation necessary to keep the spectrum analyzer from saturating, $\text{dB}_{\text{bandwidth}}$ is a correction of all spectra to a 1 Hz bandwidth. This correction is calculated using Equation B5.

$$\text{dB}_{\text{bandwidth}} = 10 \log (\Delta f/ 1 \text{ Hz}) \quad (\text{B5})$$

where Δf is the frequency range for the spectrum divided by 512 storage bins. While this is not a totally correct

procedure because it is oblivious to small frequency scale amplitude variations, it has been done so that the levels presented here can be compared to the levels obtained by other investigations which also correct to 1 Hz bandwidth routinely.

As described in section 3.6, a LC-10 hydrophone was used as a sound source next to the model. The free field transmitting response of the LC-10 due to a white noise excitation was obtained in an anechoic calibration tank at ARL/PSU using gated tone bursts. This response is shown in Figure B1. Figure B2 shows the receiving calibration for the hydrophone. Note that the sensitivity is fairly uniform over the 1 - 100 kHz frequency range.

The response of the receiving LC-10 hydrophone to acoustic white noise generated in the vicinity of the model nose was found by subtracting Figure B1 from the received spectrum and making the other corrections given by Equation B1 to develop the sensitivity spectrum of Figure B3.

The receiver response to cavitation and tunnel noise is corrected with the attenuation and gain levels and for bandwidth. The sensitivity spectrum was subtracted from this receiver spectrum to yield an absolute dB re 1 μ Pa level for the receiver response to cavitation noise spectrum. Figure B4 shows a typical final spectrum.

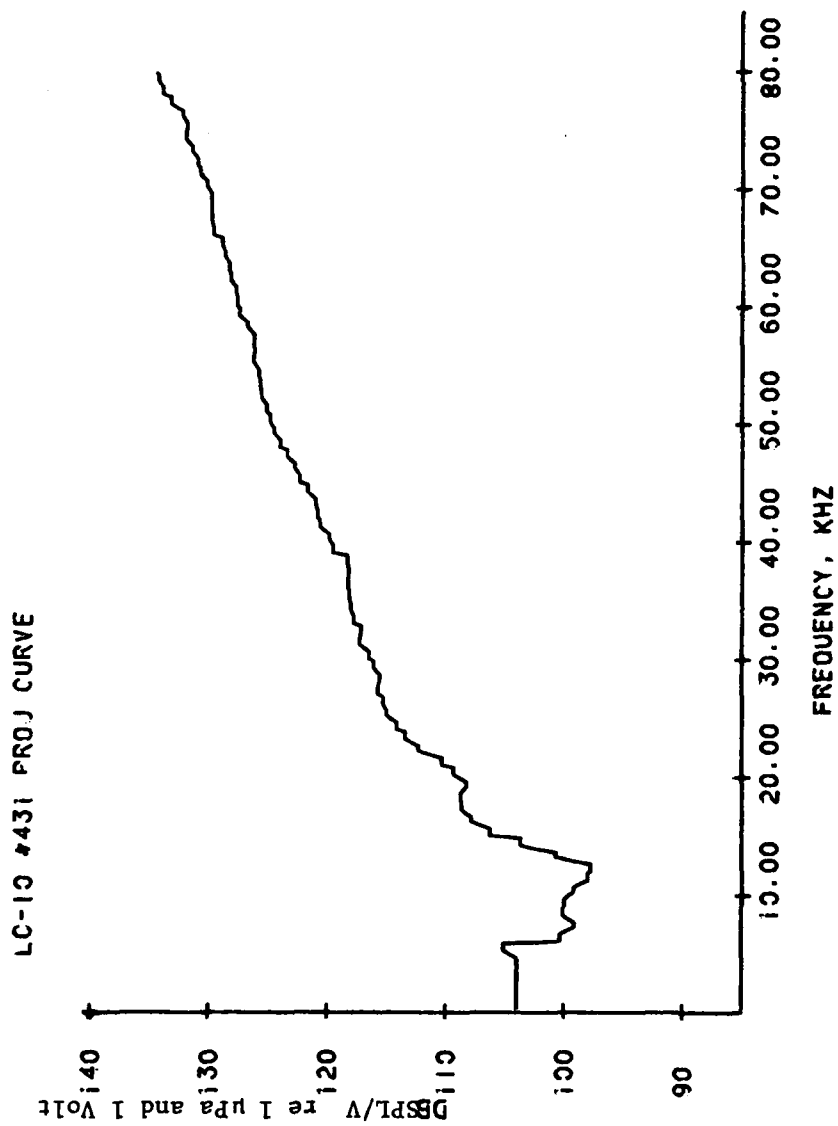


Figure B1. LC-10 Free Field Transmitting Response.

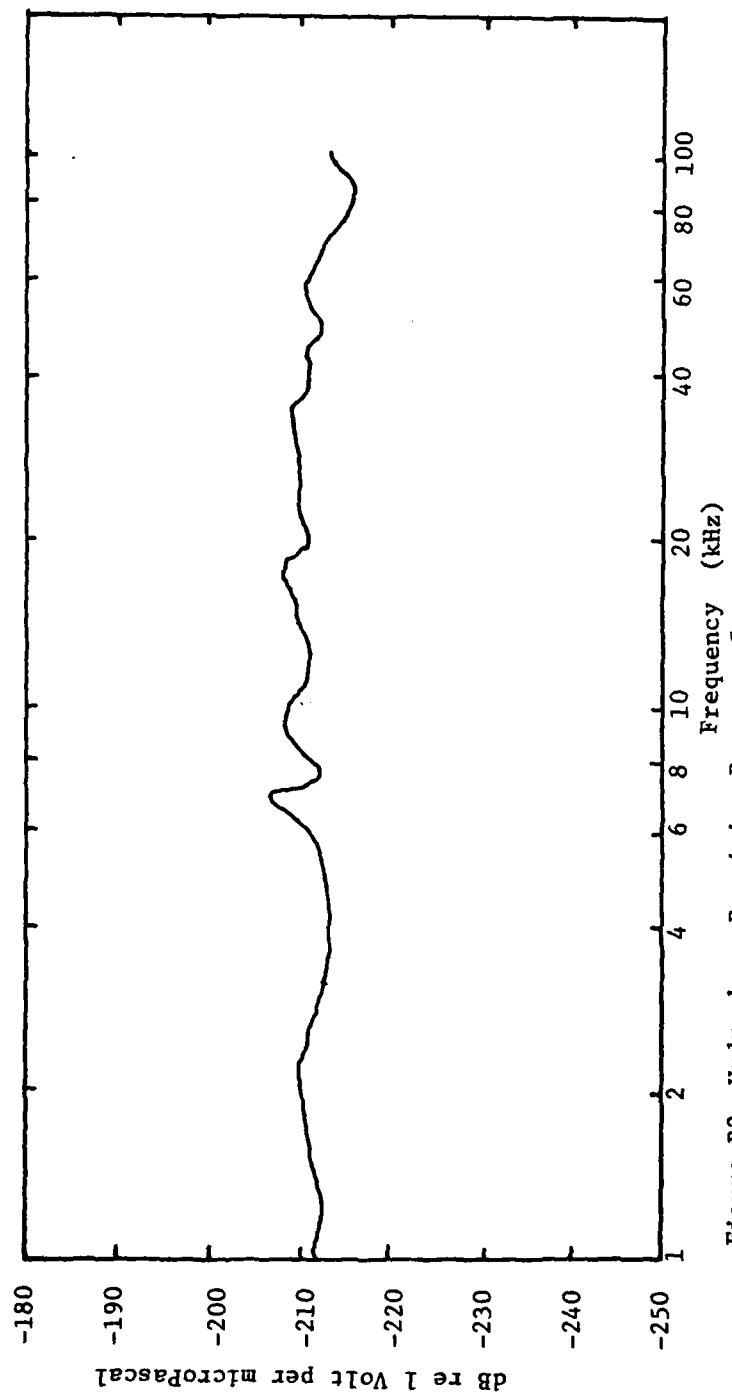


Figure B2. Hydrophone Receiving Response Spectrum.

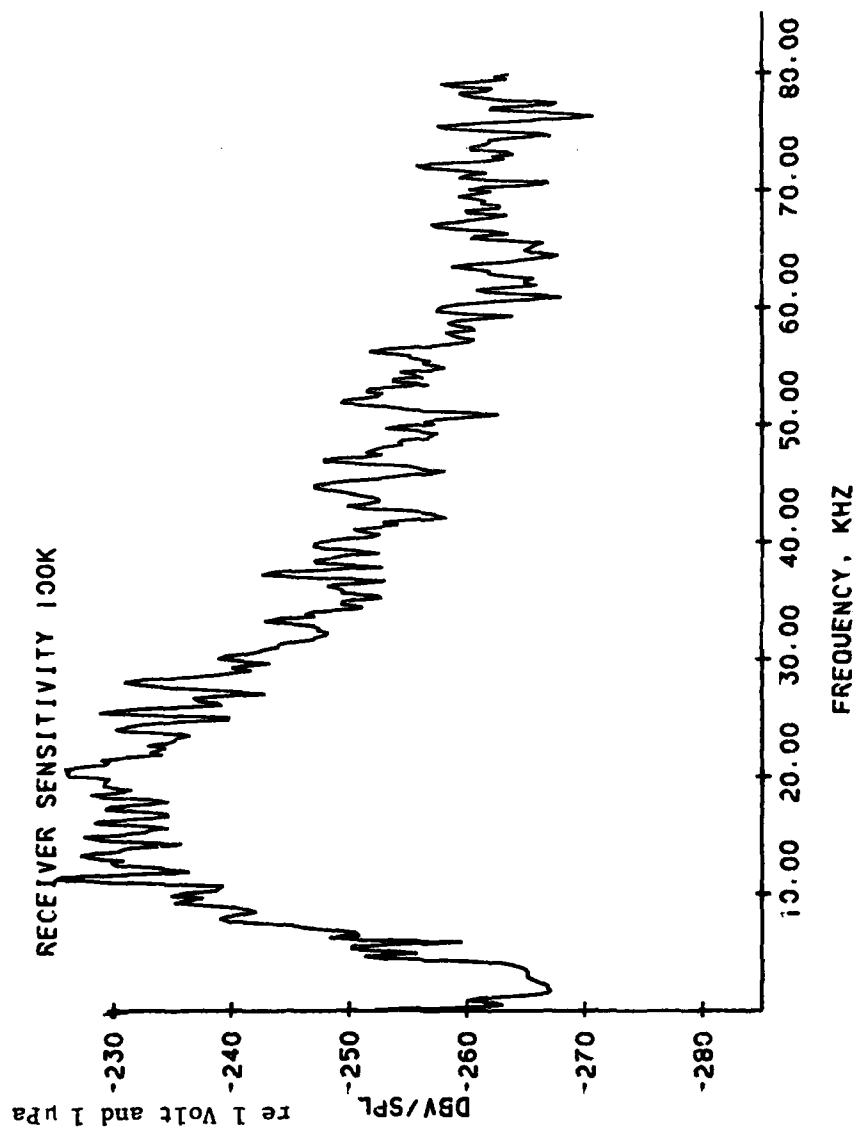


Figure B3. Sensitivity Spectrum.

VEL-37.5 SIGMA- .80

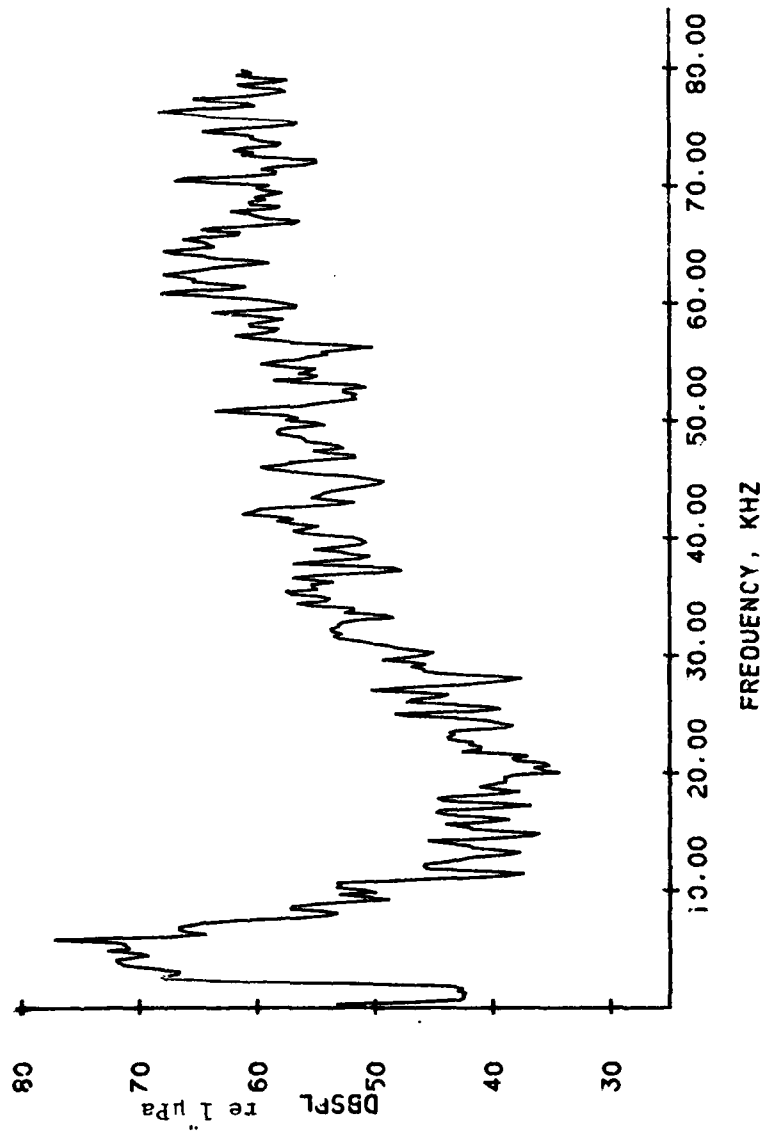


Figure B4. Typical Cavitation Noise Spectrum.

DISTRIBUTION LIST FOR ARL UNCLASSIFIED TM No. 82-94 by R. C. Marboe, dated April 13, 1982.

Commander
Naval Sea Systems Command
Department of the Navy
Washington, DC 20362
Attn: S. M. Blazek
Code NSEA-05HB
(Copy No. 1)

Naval Sea Systems Command
Attn: H. C. Claybourne
Code NSEA-05H5
(Copy No. 2)

Naval Sea Systems Command
Attn: J. H. Huth
Code NSEA-05DC2
(Copy No. 3)

Naval Sea Systems Command
Attn: F. E. Eissing
Code NSEA-05H
(Copy No. 4)

Naval Sea Systems Command
Attn: E. G. Liszka
Code NSEA-63R1
(Copy No. 5)

Naval Sea Systems Command
Attn: T. E. Peirce
Code NSEA-63R31
(Copy No. 6)

Naval Sea Systems Command
Attn: A. R. Paladino
Code NSEA-05H1
(Copy No. 7)

Naval Sea Systems Command
Attn: F. Romano
Code NSEA-05H
(Copy No. 8)

Commanding Officer
Naval Underwater Systems Center
Newport, RI 02840
Attn: D. Goodrich
Code 3634
(Copy No. 9)

Naval Underwater Systems Center
Attn: T. A. Davis
Code 36314
(Copy No. 10)

Naval Underwater Systems Center
Attn: R. J. Kittredge
Code 3634
(Copy No. 11)

Naval Underwater Systems Center
Attn: R. Trainor
Code 36314
(Copy No. 12)

Naval Underwater Systems Center
Attn: P. Corriveau
(Copy No. 13)

Commanding Officer
Naval Ocean Systems Center
San Diego, CA 92152
Attn: D. Nelson
Code 6342
(Copy No. 14)

Commander
David W. Taylor Naval Ship R&D Center
Department of the Navy
Bethesda, MD 20084
Attn: W. K. Blake
Code 1905
(Copy No. 15)

David W. Taylor Naval Ship R&D Center
Attn: T. E. Brockett
Code 1544
(Copy No. 16)

David W. Taylor Naval Ship R&D Center
Attn: R. W. Brown
Code 1942
(Copy No. 17)

David W. Taylor Naval Ship R&D Center
Attn: R. A. Cumming
Code 1544
(Copy No. 18)

David W. Taylor Naval Ship R&D Center
Attn: T. M. Farabee
Code 1942
(Copy No. 19)

David W. Taylor Naval Ship R&D Center
Attn: F. E. Geib
Code 1942
(Copy No. 20)

DISTRIBUTION LIST FOR ARL UNCLASSIFIED TM No. 82-94 by R. C. Marboe, dated April 13, 1982.

David W. Taylor Naval Ship R&D Center
Attn: J. H. McCarthy
Code 154
(Copy No. 21)

David W. Taylor Naval Ship R&D Center
Attn: T. C. Mathews
Code 1942
(Copy No. 22)

David W. Taylor Naval Ship R&D Center
Attn: W. B. Morgan
Code 15
(Copy No. 23)

David W. Taylor Naval Ship R&D Center
Attn: K. D. Remmers
Code 1942
(Copy No. 24)

David W. Taylor Naval Ship R&D Center
Attn: M. M. Sevik
Code 19
(Copy No. 25)

David W. Taylor Naval Ship R&D Center
Attn: J. Shen
Code 194
(Copy No. 26)

Commander
Naval Surface Weapons Center
Silver Spring, MD 20910
Attn: G. C. Gaunard
Code R-31
(Copy No. 27)

Office of Naval Research
Department of the Navy
800 N. Quincy Street
Arlington, VA 22217
Attn: M. M. Reischmann
(Copy No. 28)

Office of Naval Research
Attn: H. Fitzpatrick
Code 438
(Copy No. 29)

Defense Technical Information Center
5010 Duke Street
Cameron Station
Alexandria, VA 22314
(Copy Nos. 30 to 35)

Dr. Bruce D. Cox
Hydrodynamics Research Assoc., Inc.
7900 Inverness Ridge Road
Potomac, MD 20954
(Copy No. 36)

Allis-Chalmers Corp.
Hydro-Turbine Division
Box 712
York, PA 17405
Attn: R. K. Fisher
(Copy No. 37)

Rand Corporation
1700 Main Street
Santa Monica, CA 90406
Attn: C. Gazley
(Copy No. 38)

Netherlands Ship Model Basin
Haagsteeg 2
P.O. Box 28
67 AA Wageningen
The Netherlands
Attn: Mr. J. van der Kooij
(Copy No. 39)

Netherlands Ship Model Basin
Attn: Dr. J. van der Meulen
(Copy No. 40)

Netherlands Ship Model Basin
Attn: G. Kuiper
(Copy No. 41)

Dr. Albrecht
Forschungsbeauftragter für Hydroakustik
8012 Ottobrunn B Munchen
Waldparkstr. 41
Munich Germany
(Copy No. 42)

Mr. H. J. Baiter
Fraunhofer-Institut für Hydroakustik
Postfach 260
8012 Ottobrunn
Fed. Rep. of Germany
(Copy No. 43)

Dr. Ir. A. De. Bruijn
Technisch Physische Dienst TNO-TH
Stieltjesweg 1
Postbus 155
Delft
The Netherlands
(Copy No. 44)

DISTRIBUTION LIST FOR ARL UNCLASSIFIED TM No. 82-94 by R. C. Marboe, dated April 13, 1982.

Dr. Allen Moore
Admiralty Research Laboratory
Teddington, Middlesex
England
(Copy No. 45)

Dr. Weitendorf
HSVA
Hamburg
Germany
(Copy No. 46)

Von Karman Inst. for Fluid Dynamics
Turbomachinery Laboratory
Rhode-Saint-Genese
Belgium
Attn: Library
(Copy No. 47)

Dr. V. H. Arakeri
Department of Mechanical Engineering
Indian Institute of Science
Bangalore 560 012
India
(Copy No. 48)

Institute of High Speed Mechanics
Tohoko University
Sendai
Japan
(Copy No. 49)

Dr. Allan J. Acosta
California Institute of Technology
Division of Engineering for
Applied Sciences
Pasadena, CA 91109
(Copy No. 50)

Dynamics Technology, Inc.
3838 Carson Street, Suite 110
Torrance, CA 90503
Attn: Wayne H. Haigh
(Copy No. 51)

Bolt, Beranek and Newman
50 Moulton Street
Cambridge, MA 02136
Attn: Dr. N. A. Brown
(Copy No. 52)

Prof. Patrick Leehey
Dept. of Ocean Engineering - Room 5-222
Massachusetts Institute of Technology
77 Massachusetts Avenue
Cambridge, MA 02139
(Copy No. 53)

Naval Postgraduate School
The Presidio
Monterey, CA 93940
Attn: Library
(Copy No. 54)

Dr. Roger E. A. Arndt
St. Anthony Falls Hydraulic Laboratory
University of Minnesota
Mississippi River at 3rd Ave., S.E.
Minneapolis, MN 55414
(Copy No. 55)

Defense Advanced Research Projects Agency
1400 Wilson Boulevard
Arlington, VA 22209
Attn: P. Selwyn, T10
(Copy No. 56)

Creare, Inc.
~~Box 71~~
Hanover, NH 03755
Attn: W. Swift
(Copy No. 57)

Hydronautics, Inc.
Pindell School Road
Laurel, MD 20810
(Copy No. 58)

Applied Research Laboratory
The Pennsylvania State University
Post Office Box 30
State College, PA 16801
Attn: R. E. Henderson
(Copy No. 59)

Applied Research Laboratory
Attn: G. C. Lauchle
(Copy No. 60)

Applied Research Laboratory
Attn: D. E. Thompson
(Copy No. 61)

DISTRIBUTION LIST FOR ARL UNCLASSIFIED TM No. 82-94 by R. C. Marboe, dated April 13, 1982.

Applied Research Laboratory
Attn: E. G. Taschuk
(Copy No. 62)

Applied Research Laboratory
Attn: J. W. Holl
(Copy No. 63)

Applied Research Laboratory
Attn: M. L. Billet
(Copy No. 64)

Applied Research Laboratory
Attn: D. R. Stinebring
(Copy No. 65)

Applied Research Laboratory
Attn: R. S. Moyer
(Copy No. 66)

DATE
FILMED
7-8